Master Thesis

Rational Assembly of Organic / Inorganic Hybrid Photoanode for Solar Water Oxidation

Yeongkyu Choi

Department of Chemistry

Graduate School of UNIST

2018

Rational Assembly of Organic / Inorganic Hybrid Photoanode for Solar Water Oxidation

Yeongkyu Choi

Department of Chemistry

Graduate School of UNIST

Rational Assembly of Organic / Inorganic Hybrid Photoanode for Solar Water Oxidation

A thesis submitted to the Graduate School of UNIST
in partial fulfillment of the requirements for the degree of
Master of Science

Yeongkyu Choi

11. 21. 2017
Approved by

_____

Advisor
Byeong-Su Kim

Rational Assembly of Organic / Inorganic Hybrid Photoanode for Solar Water Oxidation

Yeongkyu Choi

This certifies that the thesis/dissertation of Yeongkyu Choi is approved.

11. 21. 2017

_____

Advisor: Prof. Byeong-Su Kim

_____

Prof. Tae-Hyuk Kwon

_____

Prof. Jungki Ryu

Abstract

A novel water oxidation photoanode based on hematite has been fabricated by rational assembly considering the property and energy level of the materials. The precisely designed catalytic multilayer composed of graphene oxide (GO) nanosheets and cobalt polyoxometalate (Co-POM) ($(GO/Co\text{-}POM)_n$) enhanced the photocatalytic efficiency and provided a high photoelectrochemical stability to the hematite electrode. This highly ordered architecture was fabricated by layer-by-layer assembly and the polymeric base layer was deposited to serve the adhesion between catalytic multilayer and hematite electrode. Compared to the bare hematite electrode, the $(GO/Co\text{-}POM)_9$ electrode exhibited 2.9 times higher hydrogen and oxygen gases generation efficiency and a huge cathodic shift of onset potential (> 380 mV) even at neutral pH conditions. Surprisingly, polymeric base layer deposited prior to catalytic multilayers improved the performance even more by facilitating the transfer of photogenerated holes for water oxidation through modification of the work function of the underlying photoelectrode. We anticipate that this unique approach will provide new insights into the design of highly efficient photoanode. The new water-based photocatalytic oxidation based on hematite has been produced by rational fabrication taking into account the material properties and energy levels.

Contents

List of Figures

Figure 8. Synthetic procedure for GO and amine-functionalized GO.

Figure 9. Scheme containing various applications of polyoxometalate.

Figure 10. Schemes and graphs describing the work function tuning. (a) Work function changes, related to various bare electrode and polymer deposited electrode. (b) LED and solar cell devices with various polymer layer depositio. (c) Work function change in layer-by-layer system and scheme for showing Work function change caused by a dipole layer terminated in positive charge.

Figure 11. ζ-potential change graph of (a) GO (-), (b) GO (+), and (c) Co-POM at different pHs.

Figure 12. Deposition of the catalytic multilayer of $(PEI/PAA)_3/(GO/Co\text{-}POM)_n$ on substrate. The morphology of the hematite electrode was observed by SEM (a) before and (b) after the deposition of $(PEI/PAA)_3/(GO/Co\text{-}POM)_9$. (c) The photograph and (d) the UV/Vis absorbance spectra of multilayer films of $(PEI/PAA)_3/(GO/Co\text{-}POM)_n$ on quartz substrates. The inset in (d) shows the linear growth of the characteristic absorption peak of GO with increasing number of bilayers (BL, *n*). The thickness and the mass of the deposited film were measured by (e) ex-situ ellipsometry and (f) in-situ QCM analysis.

Figure 13. STEM characterization of the $(GO/Co\text{-}POM)_9$ multilayer films. (a) Cross-sectional STEM image of the $(GO/Co\text{-}POM)_9$ multilayer films for EDS mapping (b) Elemental mapping of the $(GO/Co\text{-}POM)_9$ multilayer films, obtained from an EDS scan of the yellow box in panel (a). (c) High-magnification STEM image of the $(GO/Co\text{-}POM)_{10}$ multilayer films used for EELS analysis. (d) EELS line scan corresponding to the multilayer films. The blue and black lines correspond to the W and C, respectively, in GO and Co-POM layers extracted from the W O edge and C K edge peaks at 36 eV and 284 eV, respectively. (e-i) Extracted EELS data on different positions of multilayer: (e-f) C K edge and W O edge spectra on a GO layer, respectively; (g-h), C K edge and W O

edge spectra on a Co-POM layer, respectively and (i) Fe M edge spectra on the hematite electrode.

Figure 14. Photoelectrochemical performance of the hematite photoanode with the catalytic multilayers investigated by (a, b) LSV, (c) photocurrent measurement, and (d) gas chromatography. (a) Effect of the thermal reduction of GO on the performance of the hematite photoanode in the presence of the polymeric base layer $(PEI/PAA)_3$ and catalytic $(GO/Co\text{-}POM)_9$ multilayers as a representative film. (b) Influence of the number of the catalytic layers (BL, *n*). LSV curves were measured in a phosphate buffer solution (pH 8, 80 mM) in the presence (solid line) and absence (dashed line) of visible light irradiation. (c) Cycling test showing the long-term stability of the catalytic multilayer films of 9- and 17 BL under the applied bias of 1.23 V *vs.* RHE. (d) Time course of H_2 and O_2 gas evolution by the hematite photoanode with $(PEI/PAA)_3/(GO/Co\text{-}POM)_9$ film under visible light irradiation.

Figure 15. XPS analysis graph of (a, b) $(GO/Co\text{-}POM)_{17}$ on hematite electrode before and after thermal reduction at 200 °C. According to XPS analysis, the ratios of C/N and C/O were increased from 4.10 and 1.57 to 8.59 and 2.47, respectively, after the reduction. The deconvoluted high-resolution XPS spectra of carbon showed the decreased fraction of the C-N (286.0 eV), C=O and C-OH (287.7 eV), while that of the C-C (284.6 eV) maintained.

Figure 16. Raman spectrum of hematite, Co-POM and before and after reduction of $(GO/Co\text{-}POM)_9$ multilayer. This graph shows that the characterization peak of hematite (223, 291, 412, and 1318 cm^{-1}) and Co-POM (810, 900, and 968 cm^{-1}) is stably included after reduction. In addition, the reduction of GO is indicated by significantly decreased ratio D (1307.5 cm^{-1}) and G (1597.8 cm^{-1}) peak from 2.38 to 1.75.

Figure 17. Photoelectrochemical performance graph. (a) Current density at hematite, base layer, $(GO/Co\text{-}POM)_n$ electrode at 0.56 V and (b) chronoamperogram measured at short time intervals.

Figure 18. Graph representing the effect of polymeric base layer on density. The red line shows the difference in current density with number of catalytic multilayer when the polymeric base layer is deposited to 3 BL. On the other hand, the block line shows when there is no polymeric base layer.

Figure 19. Energy level analysis of the hematite photoanode with the catalytic multilayers. (a) 3D plot summarizing the tendency of current density to be controlled by number of catalytic bilayers and polymeric base layers. (b) Nyquist plots of impedance for hematite electrode assembled with catalytic multilayers, (c) The changes in work functions measured by UPS spectroscopy, (d) Scheme for reduced work function due to the dipole moment induced by polymeric base layers. (e) Energy diagram of all electrodes in this study. Band-bending is omitted for simplicity.

Figure 20. Ultraviolet photoelectron spectroscopy (UPS) spectra of hematite, base layer, $(GO/Co\text{-}POM)_9$ and $(GO/Co\text{-}POM)_{17}$ electrodes. (a) Fermi level and (b) cut-off level analysis of electrodes.

List of Scheme and Table

I. Introduction

The rapid increase in energy demand has accelerated the depletion of fossil fuels and raised the proportion of greenhouse gases in atmosphere, causing global warming.[1] To address this problem, scientists have worked to develop an eco-friendly and sustainable energy system by converting sunlight, which is an infinite energy source.[3] Plants, as an ideal model system inspired to develop this system by suggesting the rationally designed and precisely assembled photosynthetic machinery in thylakoid membranes (Figure 1). It is found that the precise molecular arrangement of light-harvesting pigments, redox-active molecules, and catalytic active sites in the photosynthetic machinery ensures the efficient harvesting of sunlight and directional transfer of electrons through the machinery, resulting in high efficiency of natural photosynthesis.[4,5] Inspired by this delicacy, various types of artificial photosynthetic machinery[6–11] have been developed by developing functional materials with higher performance and finding optimum combination of functional components. For example, the photosynthetic Z-scheme can be simply mimicked by integrated system that combines a proper catalyst (e.g., redox enzymes,[8,9] electrocatalyst,[10,11] etc.) with a semiconducting materials (e.g., TiO_2,[8] Si,[9,12] Fe_2O_3,[12] etc.) (Figure 2).

In addition, the formation of the mollusk shell gave an idea on the development of a well-ordered composite material in terms of architecture. It is well-known that excellent mechanical properties of nacre are originated from its unique lamellar structure where fragile calcium carbonate crystals and soft polypeptides are hybridized at nanoscale precision.[13] The nanoscale organic/inorganic hybrid structure of nacre has inspired many researchers to develop artificial nacre films with excellent mechanical strength,[14–16] (Figure 3a) and flexibility[2] (Figure 3b) through the novel nanofabrication methods, [17,18] but has been mostly limited to mechanical applications. Considering the delicate architecture and high efficiency of the photosynthetic machinery where various organic and inorganic components are arranged at nanoscale precision, it is believed that existing researches on nacre-like system can provide new approaches to design and fabricate efficient artificial photosynthetic devices.

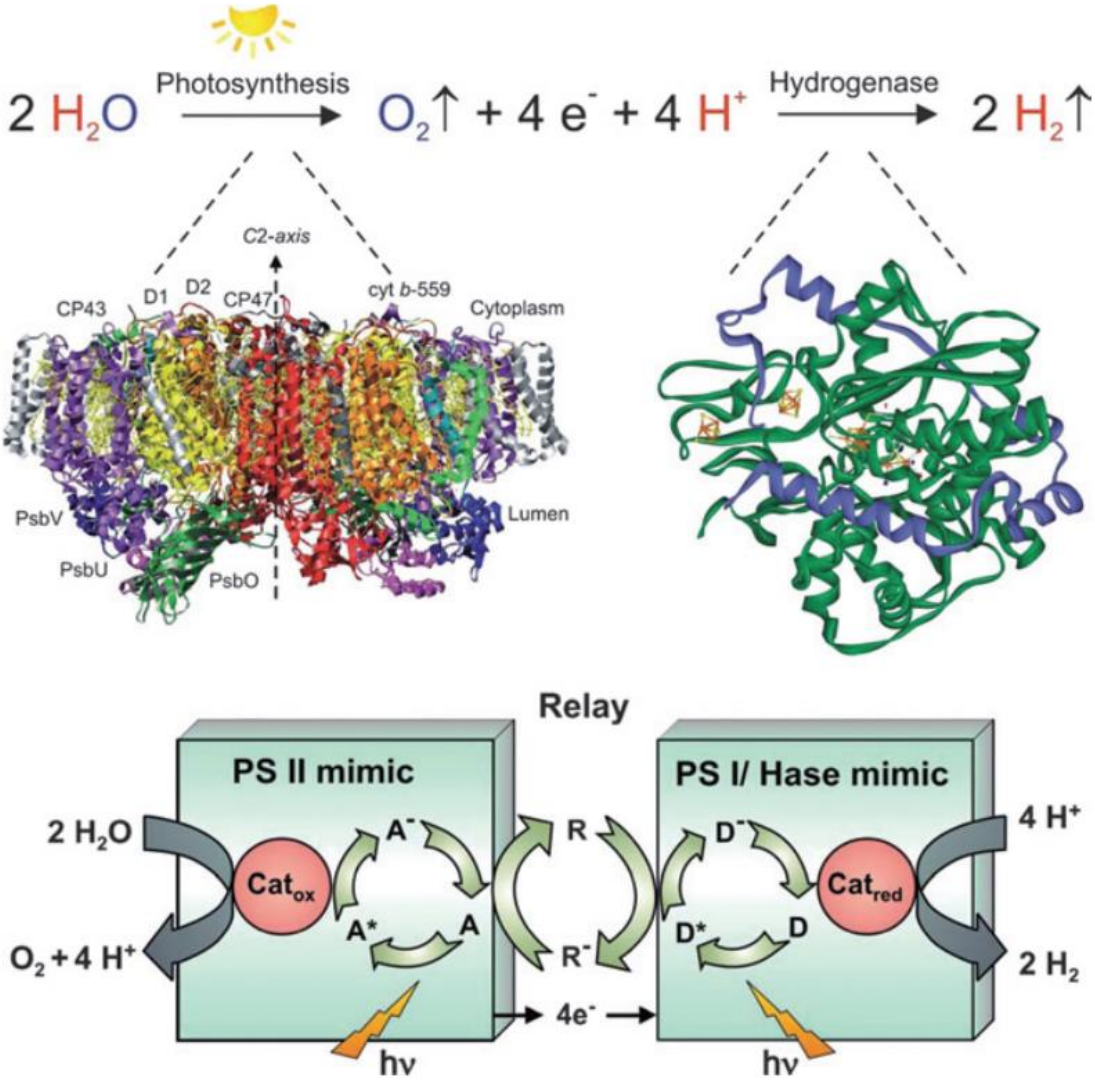

Figure 1. Scheme of light induced water splitting in photosystem II.[5] Reprinted with permission from *Energy Environ. Sci.* **2008**, *1*, 15. Copyright 2008 the Royal Society of Chemistry.

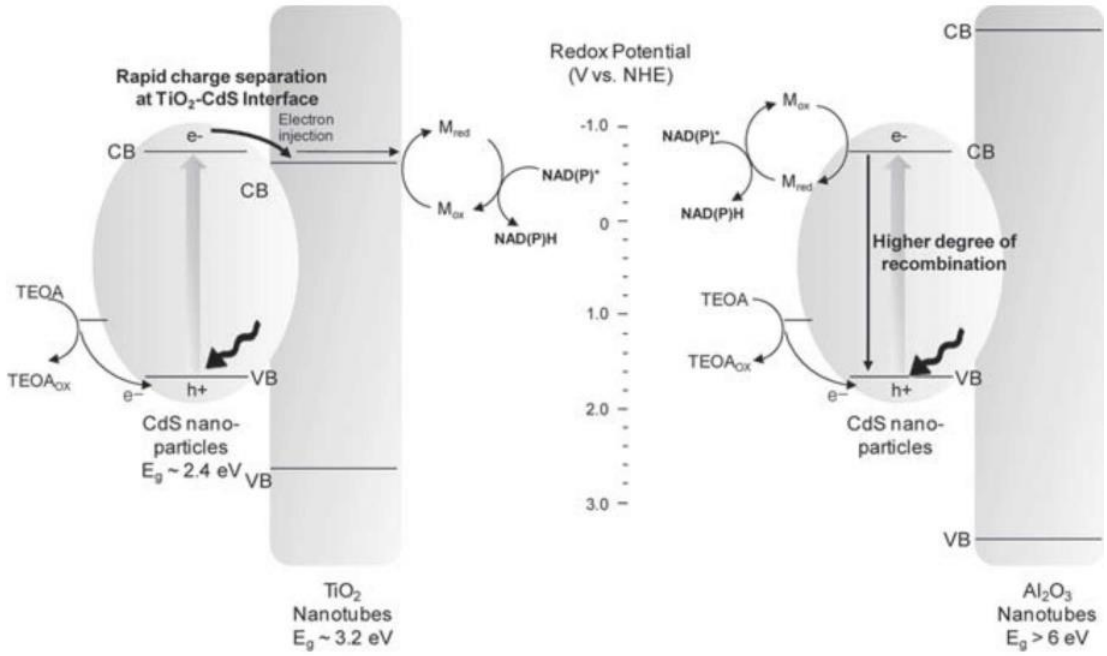

Figure 2. Schematic representation of electrons and holes transfer in integrated system that combines a proper catalyst for artificial photosynthesis by mimicking the Z-scheme.[8] Reprinted with permission from *Adv. Mater.* **2011**, *23*, 1883. Copyright 2011 WILEY-VCH.

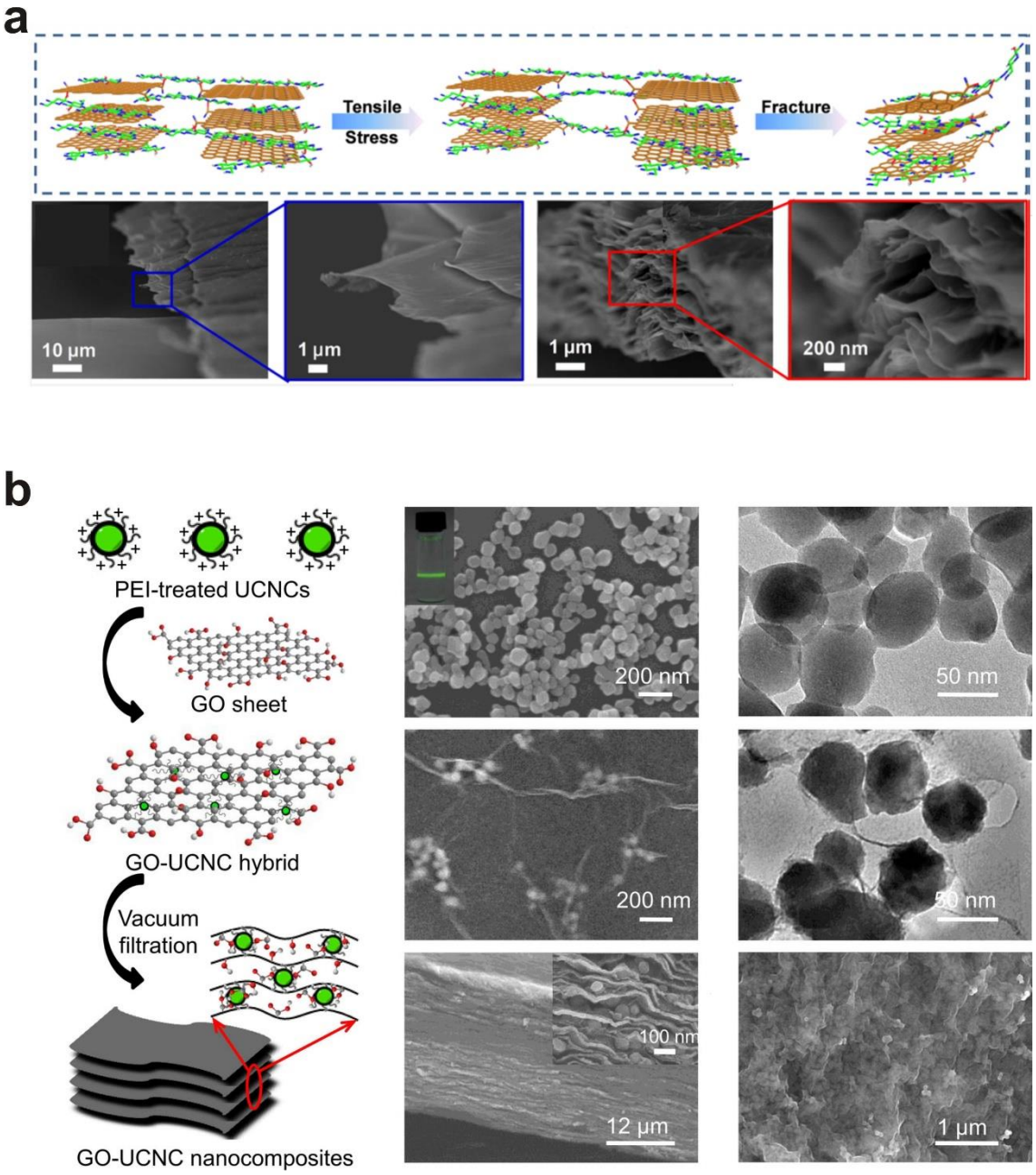

Figure 3. Synthetic schemes and TEM images of artificial nacre film. (a) GO and chitosan based nacre-like film for outstanding mechanical properties.[15] (b) Flexible multilayers integrating Fe_3O_4 Magnetic nanocrystal and lanthanide-doped upconversion nanocrystal into GO matrix.[2] Reprinted with permission from *ACS Nano* **2015**, *9*, 9830, *Adv. Eng. Mater.* **2015**, *17*, 523. Copyright 2015 American Chemical Society and 2015 WILEY-VCH.

In this regard, we designed the novel electrode with a highly organized internal nanostructure of organic/inorganic complexes to synergistically couple light-harvesting and electrocatalytic processes for efficient solar water oxidation. As a model system, we choose hematite (α-Fe_2O_3) as a photoelectrode for water oxidation due to low cost, abundance, good photochemical stability, and wide absorption range in visible light.[12,19–21] To alleviate its intrinsic limitations such as fast recombination of photo-generated charge carriers (<10 ps), short hole diffusion length (2–4 nm) and the high requisite overpotential, herein, we report the fabrication of nacre-like organic/inorganic hybrid films on hematite through the facile, solution-based layer-by-layer assembly for efficient solar water oxidation. Specifically, we choose graphene oxide (GO) nanosheets and cobalt based polyoxometalate ($[Co_4(H_2O)_2(PW_9O_{34})_2]^{10-}$, Co-POM) as a key catalytic component due to the respective role in effective charge transfer,[22,23] fast water oxidation electrocatalysis.[24] In addition, we investigated the synergetic effect of each component through the control over the internal nanostructure of the electrode. Furthermore, a specific polymeric base layer consisting of poly(ethylene imine) (PEI) and poly(acrylic acid) (PAA) was introduced in solar water oxidation system to induce dipole moment change on the electrode surface, which resulted in significantly improved charge transport through work function tuning. In this study, we fabricated the highly efficient organic/inorganic photosynthetic devices by exploiting well-ordered artificial nacre-like nanostructure and tuning the work function of the underlying electrode via a simple solution process. We anticipate that this study will provide a novel platform to assemble various nanoscale components to design high performance multiscale hybrid photocatalysts.

1-1. Water Splitting Reaction

Water splitting reaction is a clean energy conversion system that convert solar energy into chemical energy. In this reaction, water is divided into hydrogen and oxygen through the light-derived electron transfer. During this reaction, photocatalyst plays a crucial role in the absorption of solar energy and convert solar energy into chemical energy with minimal energy loss (Figure 4a).[25] The energy barrier that must be exceeded

when occurring water splitting reaction is theoretically 1.23 eV, which actually requires more energy and the photocatalyst uses light energy to drive the reaction.

$$2H_2O \xrightarrow{\text{Photon energy}} 2H_2 + O_2$$

The first water-splitting photocatalyst was reported to *Nature* in the 1972 by Akira Fujishima and Kenichi Honda (Figure 4b).[26] They found that the TiO_2 electrode, a type of semiconductor, could decompose the water and generate hydrogen and oxygen gas by irradiating ultraviolet and external potentials. This experiment inspired many researchers and led to the development of various types of photocatalysts. However, semiconductor based photocatalysts showed low energy conversion efficiency due to the limited light absorption in ultraviolet range[26] and self-recombination of holes and electrons separated by light irradiation. To address these problems, researchers tried to fabricate composite which combines the semiconductor nanoparticle with metal particles. Chen *et al*. combined the gold nanoparticle on the surface of TiO_2 nanoparticle to improve the photocatalytic efficiency. Gold nanoparticles absorbed visible light through the surface plasmon resonance and transferred excited electrons to TiO_2 (Figure 4c).[27] Meng *et al.* reported the enhanced water oxidation catalyst compared with bare hematite (α-Fe_2O_3) nanoparticle by incorporating hematite nanoparticle on the reduced graphene oxide (rGO) nanosheets instead of expensive metal nanoparticle (Figure 4d).[7] The rGO successfully hindered recombination of excited electrons and holes in hematite nanoparticle and increased the charge mobility by providing conductivity. In addition Liu *et al.* succeeded in synthesis of high efficiency water splitting photocatalyst with only carbon material. They designed photocatalysts that operated in the visible region by combining graphene quantum dots (GQDs) and carbon nitride (g-C_3N_4) (Figure 4e).[28]

1-2. Photoelectrochemical cell

A photoelectrochemical (PEC) cell, called artificial photosynthesis, is a photoelectric system for efficient water splitting reaction (Figure 5a).[29] For the effective photocatalytic reactions, this system was divided into two unique photoelectrodes.

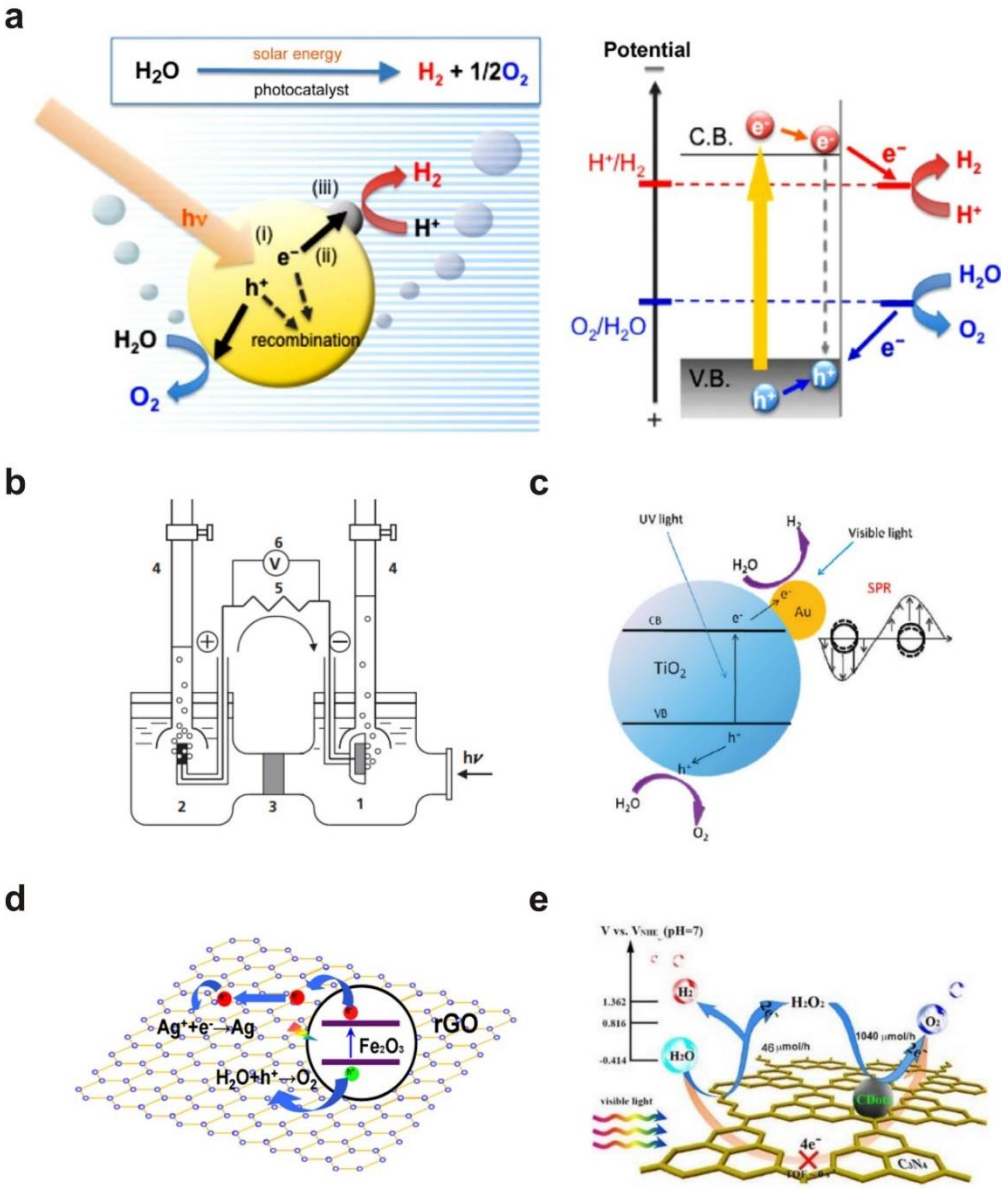

Figure 4. Researches on water splitting photocatalyst. (a) Schematic representation of water splitting catalyst and energy diagram of HER and OER. (b) The first water splitting photocatalyst system in 1972.[26] (c) Scheme of ultraviolet and visible dual-light composite photocatalyst consisted of TiO_2 with graphene quantum dots and energy diagram for charge transfer mechanism.[27] (d) Scheme of hematite nanoparticle decorated rGO water splitting photocatalyst.[7] (e) Scheme of metal free graphene quantum dot and carbon nitride based water splitting photocatalyst.[28] Reprinted with permission from *Solar Energy Materials & Solar Cells* **2014,** *128*, 85, *Nature.* **1972,** *238*, 37, *J. Phys. Chem. C* **2011**, *115*, 210, *ACS Catal.* **2013**, *3*, 746, *Science* **2015**, *347*, 970. Copyright 2014 ELSEVIER, 1972 Nature, 2011 American Chemical Society, 2013 American Chemical Society and 2015 Science.

The photocathode consisted of p-type semiconductor occurred the hydrogen evolution reaction (HER) and photoanode fabricated from n-type semiconductor catalyzed the oxygen evolution reaction (OER) by light irradiation.

$$2H^+ + 2e^- \xrightarrow{\text{Photon energy}} 2H_2 \qquad \text{(HER)}$$

$$2H_2O \xrightarrow{\text{Photon energy}} 4H^+ + O_2 + 4e^- \qquad \text{(OER)}$$

Various studies have been carried out to fabricate an effective PEC electrode. Brillet *et al*. fabricated the porous hematite electrode through the SiO_2 encapsulation for efficient water oxidation photoanode (Figure 5b).[30] Porous hematite electrodes served enhanced surface area and as a result, this device showed 1.5 times higher photocurrent than hematite electrodes without SiO_2 encapsulation. In addition, Amal and coworkers reported the rGO decorated bismuth vanadate ($BiVO_4$) for improving its photo response and fast electron transfer in visible light (Figure 5c).[31]

1-3. Hematite electrode

Hematite electrode has attracted great attention as an ideal artificial photosynthesis material due to many advantages as photoanode for water oxidation catalyst including low cost, excellent photochemical stability, suitable band gap (2.2 eV), reasonable conversion efficiency, and broad absorption range at visible light, but it is hindered by fast recombination because of the short lifetime of photo-generated charge carrier (<10 ps), short hole diffusion length (2-4 nm). To address this limitation, many methods have been developed by engineering morphology control,[19] heteroatomic doping, and hybrid system with carbon materials such as semiconductor,[32] graphene oxide.[7] In this study, we selected the hematite electrode as basis electrode and designed the catalytic multilayer on hematite electrode to solve the intrinsic problems of hematite.

1-4. Layer-by-Layer Assembly

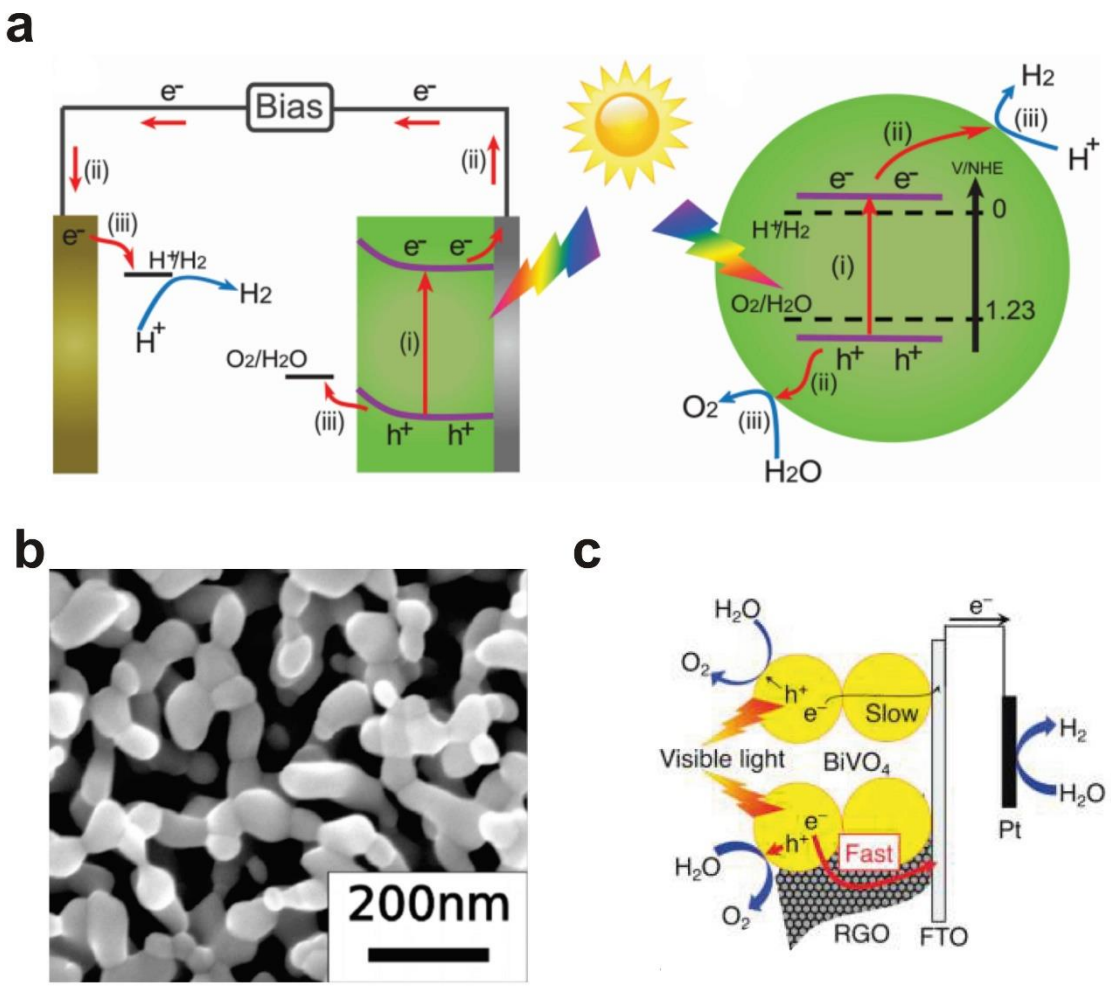

Figure 5. (a) Scheme for showing photoelectrochemical cell system for water splitting reaction.[29] (b) Scanning electron microscopy (SEM) photograph of porous hematite.[30] (c) Scheme of $BiVO_4$ decorated rGO photoanode.[31] Reprinted with permission from *Adv. Mater.* **2013**, *25*, 3820, *Nano Lett.* **2010**, *10*, 4155 and *J. Phy. Chem. Lett.* **2010**, *1*, 2607. Copyright 2013 WILEY-VCH and 2010 American Chemical Society.

Layer-by-Layer Assembly is one of the versatile technique for thin film fabrication in which a composite structure is assembled through the sequential adsorption of different materials by intermolecular interaction between components such as electrostatic interaction, hydrogen bond, and van der Waals forces (Figure 6).[33] Layer-by-Layer assembly methods include dip coating, spray coating, and spin coating. All these methods are similar in that they form layers sequentially, but they show different 3-dimensional structures because the layers are deposited by different techniques. An important step in the layer-by-layer assembly is the cleaning step performed between the coatings of the materials, which removes the loosely bound materials to help create a uniform and well-aligned layered structure. The possibility of layer-by-layer assembly of both materials can be confirmed simply by confirming cohesion between the two components or by measuring the zeta potential.

The layer-by-layer assembly can be utilized to fabricate the hybrid materials with strong physical properties, to design electrochemical or photoelectrochemical electrodes, and to develop biomaterials. For example, Kotov group fabricated a biomimetic structure through the hydrothermal growth of ZnO nanowires, followed by layer-by-layer assembly of poly(arylamine) (PAAm) and poly(acrylic acid) (PAA) for structure with high physical properties.[14] Ann *et al*. reported the electrocatalytic thin film electrodes for HER through the precisely controlled layer-by-layer assembly of MoS_2 and multiwalled carbon nanotube (MWNT).[34] In addition, Guo *et al*. fabribated glucose-responsive nanocapsule by layer-by-layer assembly of modified chitosan and randon glycopolymer. They successfully delivered the insulin loaded nanocapsules to target cell.[35]

1-5. Graphene oxide

Graphene oxide (GO) has attracted a great attention as an oxygenated graphene analog because it is cost effective, large scale producible and easily processible materials. Therefore, various studies utilizing the characteristics of GO have been reported. Park *et al*. reported the covalently functionalized GO with amine residues for oxygen reduction electrocatalyst (Figure 7a).[36] They emphasized that the heteroatomic such as a nitrogen, sulfur and boron doping improved the electrical properties of graphene and surprisingly increased the catalytic active site with a charge polarization. They reported the surface

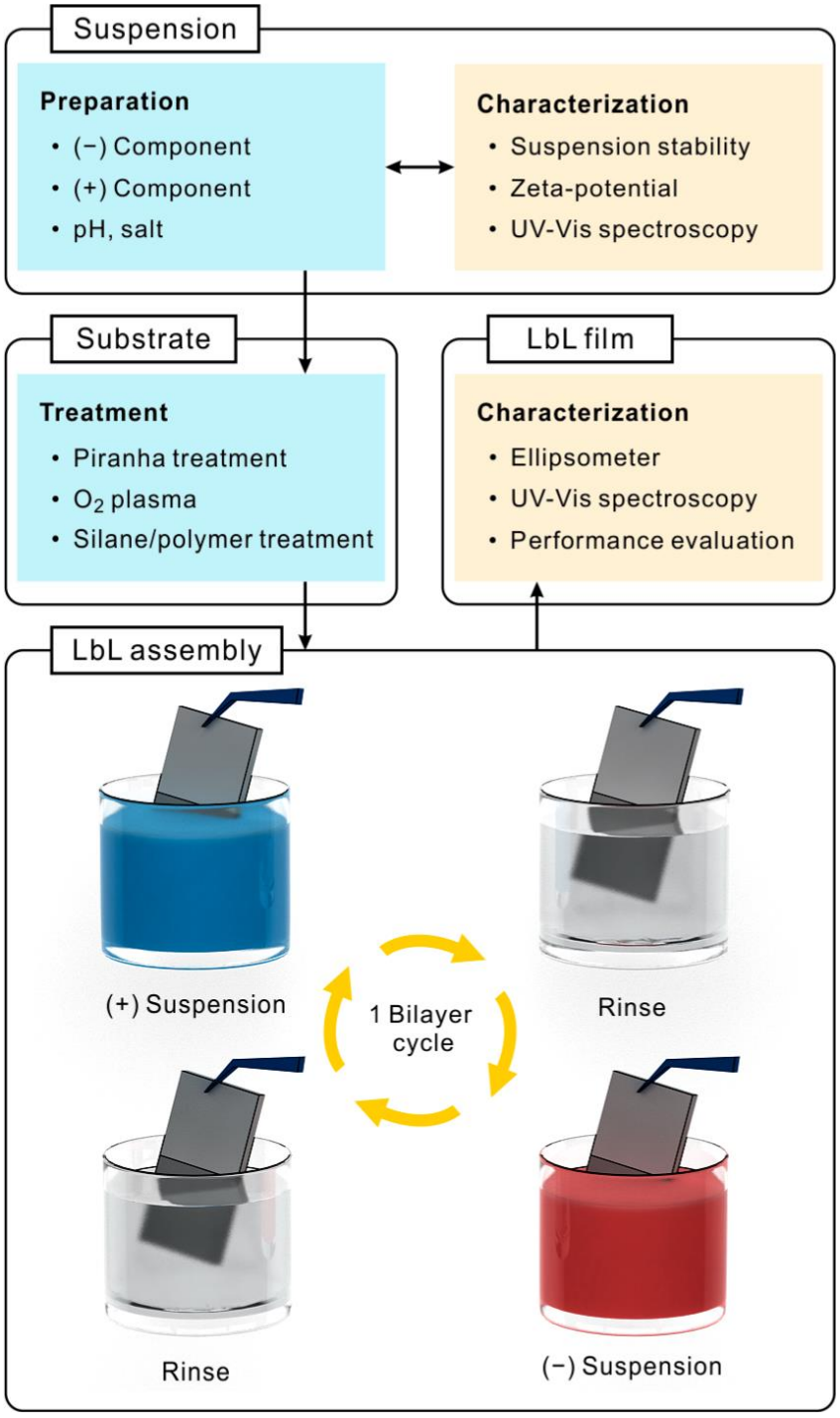

Figure 6. Schematic representation of layer-by-layer assembly steps.[34] Reprinted with permission from *Chem. Mater.* **2017**, *29*, 69. Copyright 2017 American Chemical Society.

functionalization of GO nanosheets with ethylene glycol, ethanolamine and sulfanilic acid molecules to improve the dispersion stability in various solvents (Figure 7b).[37] In addition, GO is one of the potential materials in layer-by-layer assembly field as a negative and even positive component. Gu *et al*. successfully fabricated the Au and Pd bimetallic multilayer electrocatalyst using the GO nanosheets (Figure 7c).[38] They observed that the catalytic effect was changed by controlling the sequence of the layer-by-layer thin film. Joo *et al*. reported the GO based multilayer for enhanced photoluminescence (Figure 7d).[39] This multilayer, consisting of GO and MoS_2, showed varying intensity of fluorescence depending on the layered number. With these example, GO was widely studied as a supporting material due to the large surface area, high chemical resistance, easy processibility and high conductivity after annealing step. In particular, The GO acted as a hole and electron reservoir that temporarily holds separated charges to hinder the recombination in electrochemical catalysts or photocatalysts. Therefore, we selected GO as the supporting material to fabricate a solid, conductive and high efficient photoanode by simple process.

1-5-1. Amine functionalized GO

The GO synthesized by the modified Hummer's method is basically negatively charged when dispersed in water, but it can be transformed into a positive charge GO through 1-ethyl-3-(3-dimethylaminopropyl)carbodiimide (EDC) coupling reaction (Figure 8). [33] EDC is commercially available coupling reagent for the formation of amide bonds between carboxylic acid and amine. It is typically employed in the pH 4.0-6.0 range and the carboxylic acids in GO can be replaced with amine groups by the formation of amide bond.[40] As a by-product of the reaction, water-soluble urea is generated and it can be purified by dialysis step. For self-assembly of Co-POM with negative charge, we reformed the GO by amine functionalization. GO and Co-POM were alternatively deposited on the hematite electrode and formed the catalytic multilayers.

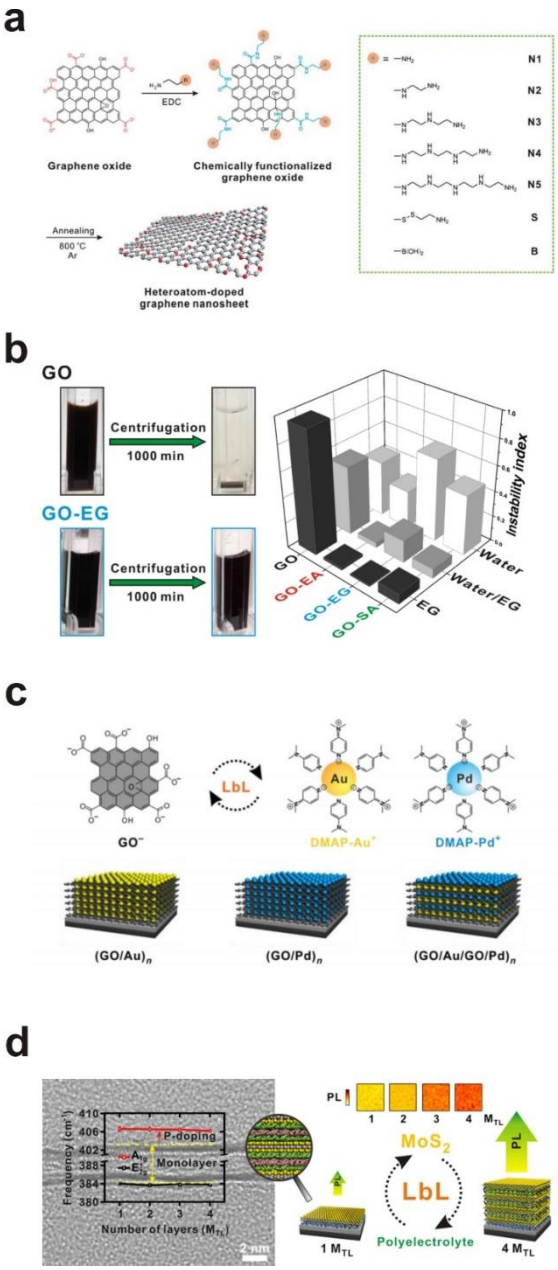

Figure 7. (a) Design and fabrication of Heteroatom-doped GO-based electrode catalysts.[36] (b) Surface functionalized GO to obtain the high dispersibility.[37] (c) Architecture control of GO, Pt and Au nanoparticle for high efficient electrocatalyst.[38] (d) Multilayer fabricated by layer-by-layer assembly with GO and MoS_2.[39] Reprinted with permission from *Nanoscale* **2013**, *5*, 12255, *ACS Appl. Mater. Interfaces* **2016**, *8*, 21595, *Nano Energy* **2016**, *30*, 658 and *Nano Lett.* **2014**, *14*, 6456. Copyright 2013 The Royal Society of Chemistry, 2017 American Chemical Society, 2016 ELSEVIER and 2014 American Chemical Society.

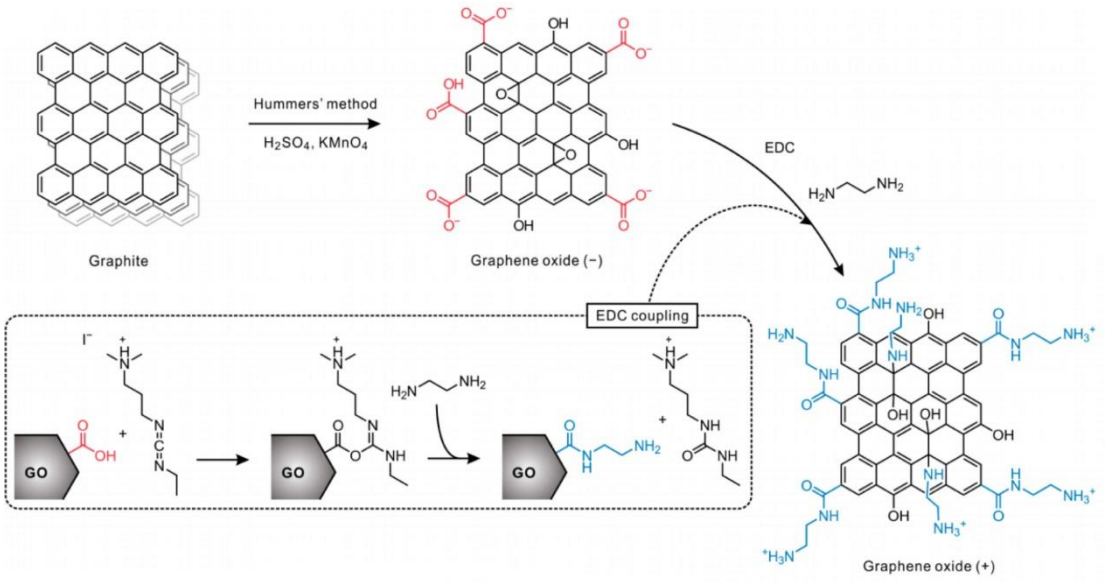

Figure 8. Synthetic procedure for GO and amine-functionalized GO.[34] Reprinted with permission from *Chem. Mater.* **2017**, *29*, 69. Copyright 2017 American Chemical Society.

1-6. Polyoxometalate

Polyoxometalate (POM) is well-defined metal-oxygen cluster anions. Since the first polyoxometalate was developed in 1826, it has been extensively studied in the fields of drag, biomass, materials development, chemical conversion catalyst, and photocatalyst for clean sustainable energy (Figure 9).[41] Among the various types of POM, especially the a fast soluble cobalt based polyoxometalate (Co-POM, ($[Co_4(H_2O)_2(PW_9O_{34})_2]^{10-}$) reported by Yin *et al*. in 2010 showed excellent photocatalytic effect. They targeted the OER and successfully observed the high performance of POM as an OER photocatalyst.[24] They used the $[(Ru(bpy)_3)]^{2+}$ as a photosensitizer to enhance the light absorption because POM could not absorb the light directly. This composite had oxidatively stabilized by polytungstate ligands structure and was a stable and efficient catalyst for water oxidation. The oxygen evolution efficiency was observed with high turnover frequencies at pH 8. After this study was published, the POM has been actively studied in the field of photocatalyst and various supporting molecule was developed to replace the expansive and unstable $[(Ru(bpy)_3)]^{2+}$. Toma *et al.* reported the photoanode that combines multiwall carbon nanotube (MWCNT) with POM for efficient water splitting.[42] POM was covalently bonded to polyamidoamine (PAMAM) ammonium dendrimers on the surface of MWCNT. Kang and coworkers designed the polyoxometalate/semiconductor composite electrode for high efficient dye sensitized solar cells (DSSCs).[43] In our photoanode system, we chose the hematite as a photosensitizer to enhance the light absorption and efficiently generate holes for delivery to POM.

1-7. Rational Assembly

We designed the photoanode consisted of hematite electrode, Co-POM, GO, poly(ethylene imine) and poly(acrylic acid) for efficient water splitting by solar energy conversion. Materials were selected to complement the limits of single material and it was arranged considering energy level and effective hole and electron transfer. Hematite was used as a photosensitizer to separate holes and electrons by light irradiation. The fast

Figure 9. Scheme containing various applications of polyoxometalate.[41] Reprinted with permission from *Chem. Rev.* **2015**, *115*, 4893. Copyright 2015 American Chemical Society.

recombination, which was a problem of hematite, was hindered by GO layer. GO temporarily stored the separated charges and transferred them to OER and HER photoelectrodes.[7]

In addition, polymeric base layer comprised of poly(ethylene imine) and poly(acrylic acid) were deposited between hematite electrode and catalytic multilayers to serve the adhesion and induce the surface dipole moment. It has already been reported in previous papers that the polymer layer deposited on the surface of electrodes induces the surface dipole and these layer enhanced the charge transfer. Zhou *et al.* reported the universal method for work function tuning by polymer layer deposition on the surface of electrodes. They described that the induced dipole moment by polymer layer changed the work function (Figure 10a).[44] Song and coworkers developed an LED and solar cell with improved performance by applying this method (Figure 10b).[45] In particular, they controlled the nitrogen content in deposited molecule and compared the change in work function. Torasso *et al.* observed the work function change in layer-by-layer system (Figure 10c).[46] They confirmed that the inducted dipole moment was determined by the charge of last deposited layer and the number of deposited layers was not affect the work function. Therefore, we firstly applied the polymeric base layer into the photoanode assembly and checked the effect of polymeric base layer in water splitting system through the work function measurement.

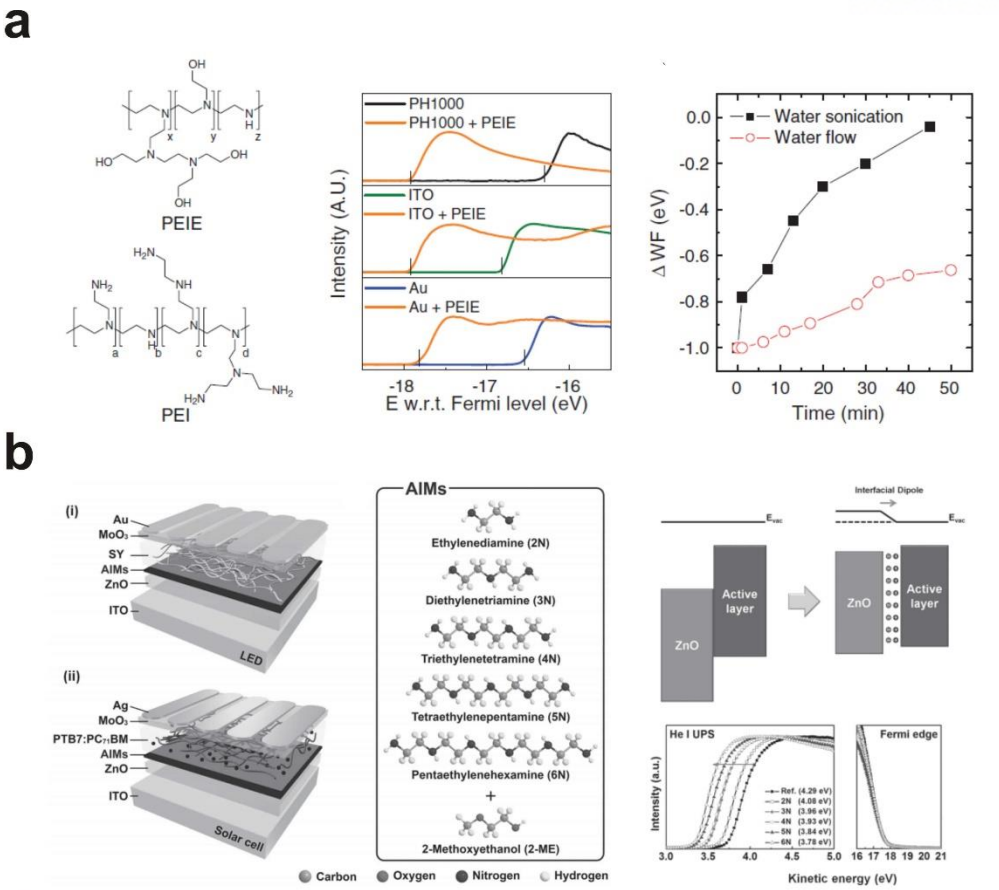

Figure 10. Schemes and graphs describing the work function tuning by polymer deposition. (a) Work function changes of bare electrodes and polymer deposited electrodes.[44] (b) LED and solar cell devices with various polymer layer deposition.[45] (c) Work function change in layer-by-layer system and scheme for showing Work function change caused by a dipole layer terminated in positive charge.[46] Reprinted with permission from *Science* **2012**, *336*, 327, *Adv. Mater.* **2015**, *27*, 3553, *Langmuir* **2017**, *33*, 2169. Copyright 2012 Science, 2015 WILEY-VCH, 2017 American Chemical Society.

II. Experiments

2-1. GO, Co-POM and Hematite Electrode Synthesis.

Graphene oxide (GO) was prepared using a modified Hummer's method and functionalized with amine group through covalent coupling with ethylene diamine in the presence of 1-[3-(dimethylamino)propyl]-3-ethylcarbodiimide methiodide. Cobalt polyoxometalate, $[Co_4(H_2O)_2(\alpha\text{-}PW_9O_{34})_2]^{10-}$ was synthesized according to the literature.[24] $Na_2WO_4{\cdot}2H_2O$, $Na_2HPO_4{\cdot}7H_2O$ and $Co(NO_3)_2{\cdot}6H_2O$ were dispersed in water and refluxed at 100 °C for two hours after adjusting the pH from 9 to 7. Then, the synthesized dark purple solution was saturated with NaCl and cooled down to room temperature for crystalization. Hematite photoanode was hydrothermally grown on fluorine-doped tin oxide (FTO) substrate according to the method described in the report Jang *et al*.[12] Fluorine-doped tin oxide (FTO) substrate was dipped in solution containing $FeCl_3$ and $NaNO_3$ and heated at 100 °C for one hour. After rince the FTO substrate, the calcination was carried out to convert the FeOOH into hematite (α-Fe_2O_3) at 800 °C for 5 min.

2-2. Deposition of Polymeric Base Layers and Catalytic $(GO/Co\text{-}POM)_n$ Layers.

Poly(ethylene imine) (PEI) (Polymer Science; M_w 10,000) and poly(acrylic acid) (PAA) solutions (Sigma Aldrich; M_w 250,000) were prepared at 5 mg/mL as cationic and anionic polyelectrolyte solutions, respectively, for the deposition of the base layers. In the case of deposition of catalytic $(GO/Co\text{-}POM)_n$ layers, GO and Co-POM solutions were prepared at 0.50 mg/mL and 1.0 mM as cationic and anionic components, respectively. Before layer-by-layer assembly, substrates were treated with oxygen plasma to increase their hydrophilicity and the pH of the solutions was adjusted to 6.0. $(PEI/PAA)_n$ base layers and subsequent $(GO/Co\text{-}POM)_n$ catalytic layers were deposited using an automatic dip-spin coater (Strato sequence IV) in the following order for the desired number of times: cationic PEI (or GO) solution for 10 min (or 3 min), deionized

(DI) water three times for 1 min each to remove any unbound polymer, anionic PAA (or Co-POM) solution for 10 min (or 3 min), and DI water three times for 1 min each. The assembled $(GO/Co\text{-}POM)_n$ multilayer films underwent thermal reduction in a tube furnace (Thermal CVD for graphene, Cyntec Co.) under the following condition: heating rate of 10 °C per min, annealing temperature of 100, 200, or 300 °C, and 4% H_2 containing argon atmosphere.

2-3. Characterization.

Surface ζ-potential of GO and Co-POM was measured to confirm the layer-by-layer condition by a ζ-potential analyzer (Malvern, Zetasizer Nano ZS). The absorbance of $(GO/Co\text{-}POM)_n$ multilayers on quartz substrate was characterized by UV−vis spectroscopy (Cary 5000, Varian). The thickness of films on silicon substrate was measured by ellipsometry (J. A. Woollam Co. Inc., EC-400 and M-2000V). The loading mass of each material absorbed onto the film surface was analyzed by quartz crystal microbalance (Stanford Research System, QCM200), according to the literature.[38] The layer-by-layer films were analyzed by X-ray photoelectron spectroscopy (XPS) and ultraviolet photoelectron spectroscopy (UPS) (Thermo Fisher, ESCALAB 250XI). The reduction state of GO was confirmed by Raman spectroscopy (Witec, Alpha300). Structural investigation including scanning electron microscopy (SEM), scanning transmission electron microscopy (STEM) images, energy-dispersive X-ray spectroscopy (EDS) mapping, and electron energy loss spectroscopy (EELS) of the $(GO/Co\text{-}POM)_n$ multilayer films was carried out using a Nova nano SEM (FEI) and a JEM-2100F HR-TEM (JEOL). Samples for STEM analysis were prepared using a dual-beam focused ion beam (FEI, Quanta 3D FEG). The energy resolution of the EELS spectrometer is about 0.9 eV as measured by the full width at half-magnitude of the zero-loss peak. The energy window of the EELS was 25-225 eV for W (W O edge, 36 eV) and Fe (Fe M edge 54 eV) peaks and 170-570 eV for C (C K edge, 284 eV) peak.

2-4. Photoelectrochemical Characterizations.

All photoelectrochemical (PEC) characterizations were carried out in 80 mM of phosphate buffer (pH 8.0). The performance of hematite-based photoanodes was evaluated by measuring linear sweep voltammogram (LSV) under visible light illumination (100 mW/cm^2) with a WMPG1000 multichannel potentiostat/galvanostat under following conditions: reference electrode, Ag/AgCl; counter electrode, Pt planar; Scan rate, 20 mV/s. A 300W Xe lamp equipped with a 400 nm cut-on filter was used as visible light source. Evolved oxygen and hydrogen gases during the PEC test were quantified with a GC-2010 Plus gas chromatograph (Shimadzu Co., Japan). Electrochemical impedance spectra were measured using a 1260 impedance analyzer (Solartron) under the following conditions: reference electrode, Ag/AgCl; counter electrode, Pt wire; applied potential of 0.5 V; amplitude, 10 mV; frequency scan range, 100 kHz to 0.1 Hz.

III. Results and discussion

3-1. Fabrication of $(GO/Co\text{-}POM)_n$ multilayers on a hematite electrode.

The catalytic multilayers of GO and Co-POM (hereafter, $(GO/Co\text{-}POM)_n$, *n* denotes the number of bilayers (BL)) were fabricated on the hematite electrode by sequential deposition of positively charged GO and negative charged Co-POM exploiting the electrostatic for solar water oxidation (Scheme 1). It is expected that GO and Co-POM can contribute to improved photoanode performance by facilitating selective and efficient transport of holes and catalytic extraction of electrons from water, respectively. Cationic GO was initially synthesized by introducing amine groups (NH_2) on chemically exfoliated GO nanosheets via covalent coupling with ethylene diamine.[33,36,40,47] In parallel, anionic Co-POM with a biomimetic oxo-bridged tetracobalt active site was prepared based on the previous report.[24] These two suspensions exhibited a considerable surface charges as indicated by the zeta-potential measurement (Figure 11). For example, GO nanosheets showed 40.1 mV and Co-POM displayed -55.7 mV at the assembly condition. Prior to the multilayer assembly, polymeric base layer composed of $(PEI/PAA)_3$ was deposited to improve the coverage and uniformity of the multilayer film on the hematite electrode. The critical role of the base layer in tuning the work function of the hematite electrode will be described more in the following discussion.

3-2. Deposition of the catalytic multilayer of $(PEI/PAA)_3/(GO/Co\text{-}POM)_n$ on substrate.

The successful assembly of $(GO/Co\text{-}POM)_n$ multilayer films was confirmed by scanning electron microscopy (SEM), UV/vis spectroscopy, ellipsometry, and quartz crystal microbalance (QCM) analysis (Figure 12). SEM images showed a significant morphological change of the hematite electrode after the assembly. While bare hematite has a worm-like structure, the deposition of the multilayers led to the formation of sheet-like structure on its surface, a characteristics of GO nanosheets, resulting in a decrease of

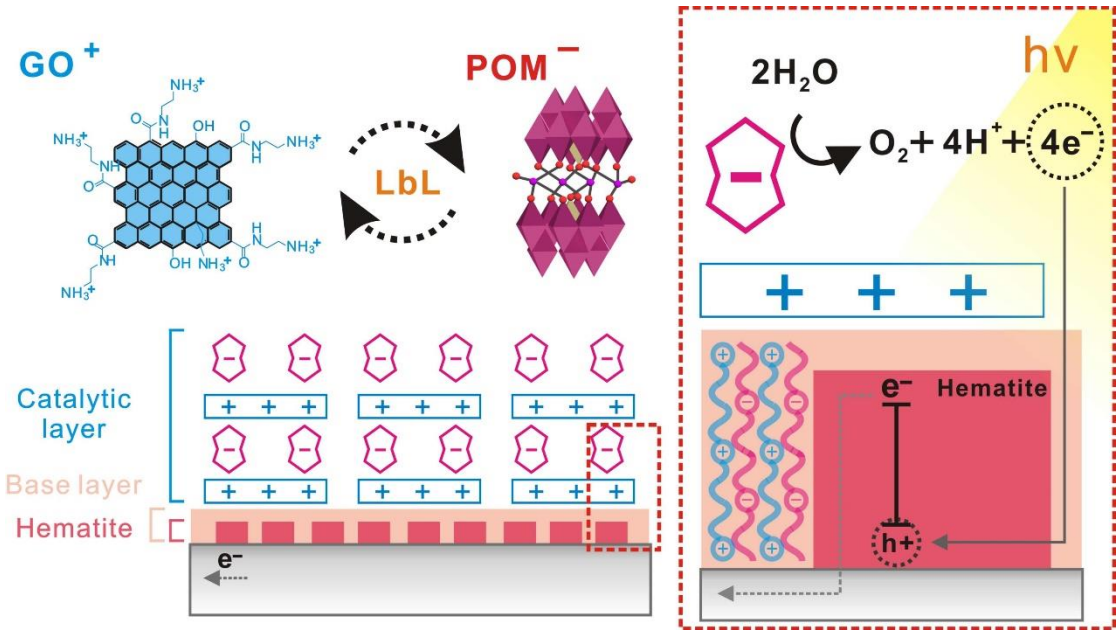

Scheme 1. Schematic representation of layer-by-layer assembled (GO/Co-POM)$_n$ multilayers on a hematite electrode with a simplified charge transfer pathway.

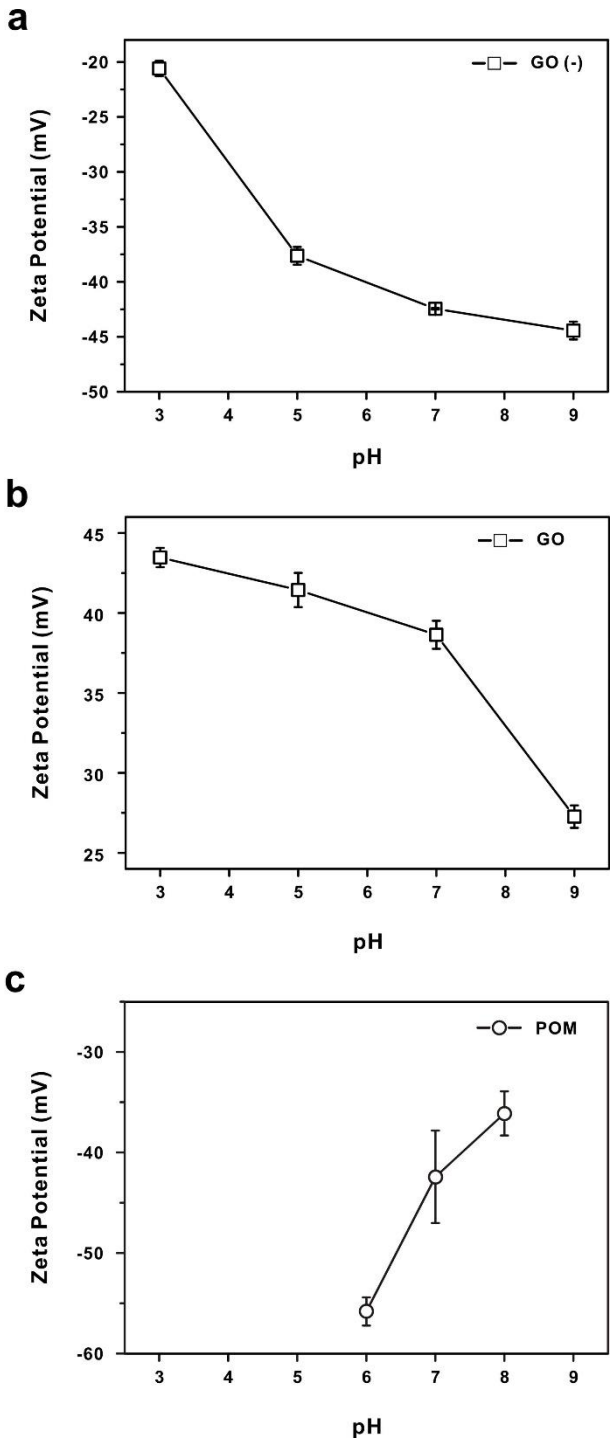

Figure 11. ζ-potential change graph of (a) GO (-), (b) GO (+), and (c) Co-POM at different pHs.

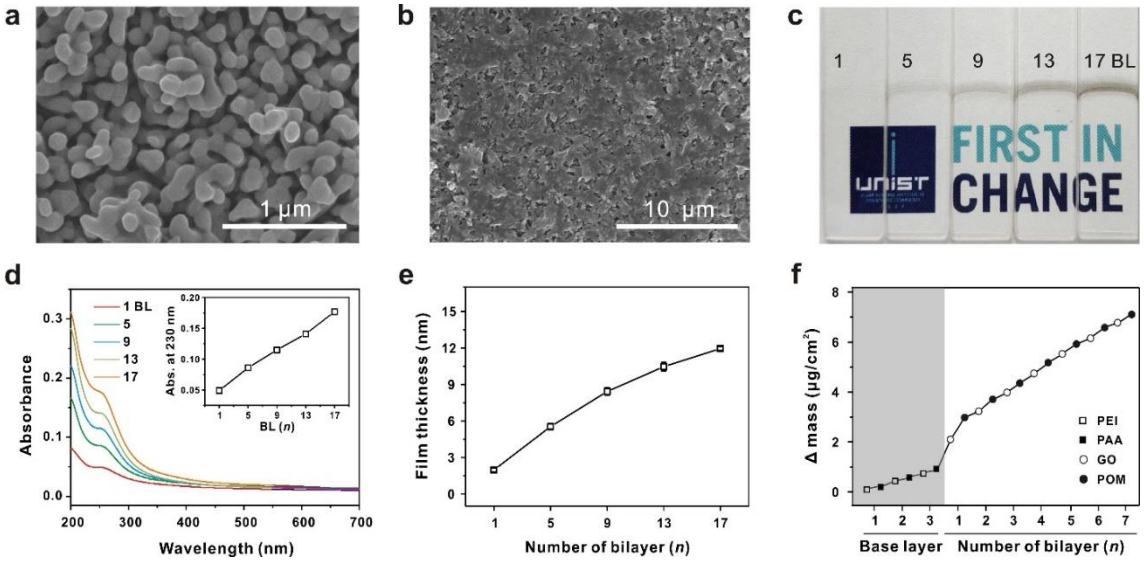

Figure 12. Deposition of the catalytic multilayer of $(PEI/PAA)_3/(GO/Co\text{-}POM)_n$ on substrate. The morphology of the hematite electrode was observed by SEM (a) before and (b) after the deposition of $(PEI/PAA)_3/(GO/Co\text{-}POM)_9$. (c) The photograph and (d) the UV/Vis absorbance spectra of multilayer films of $(PEI/PAA)_3/(GO/Co\text{-}POM)_n$ on quartz substrates. The inset in (d) shows the linear growth of the characteristic absorption peak of GO with increasing number of bilayers (BL, *n*). The thickness and the mass of the deposited film were measured by (e) ex-situ ellipsometry and (f) in-situ QCM analysis.

surface roughness (Figure 12a, b). In particular, the deposition of uniform and transparent films was clearly demonstrated through the linear growth of the characteristic peak of GO at 230 nm in the UV/vis absorption spectra (Figure 12c, d). It is of note that the transmittance of the 17 BL films reaches 93.5% at 400 nm, which corresponds to the absorption range of hematite electrode, demonstrating a negligible effect of catalytic multilayer on the light passage to hematite electrode. Ellipsometry measurement also demonstrated the uniform increase in the thickness with an average BL thickness of 0.61 ± 0.05 nm (Figure 12e). Independently, QCM analysis, which monitors the stepwise growth of the mass deposited after each layer, supported the linear growth of (GO/Co-POM)$_n$ multilayer film in a quantitative way (Figure 12f). For example, GO and Co-POM were deposited at a density of 0.25 and 0.41 μg/cm^2, respectively, in a single bilayer with a mass ratio of 1:1.6 (GO *vs*. Co-POM). The consistent growth throughout the multilayer supported the uniform deposition of each functional catalytic component such as GO and Co-POM on top of the electrode.

3-3. STEM characterization of the (GO/Co-POM)$_9$ multilayer films.

To identify the precise nanoscale architecture of the (GO/Co-POM)$_n$ multilayer film assembled on the hematite electrode, a cross-sectional scanning transmission electron microscopy (STEM), energy-dispersive X-ray spectroscopy (EDS) and electron energy loss spectroscopy (EELS) analyses of the electrode were employed as shown in Figure 13. The STEM image (Figure 13a) and the EDS elemental mapping analysis (Figure 13b) indicated that the hybrid multilayer film of (GO/Co-POM)$_n$ with W and P was deposited evenly on the ragged and wormlike hematite electrode with F and O elements. The high-magnification STEM image showed the alternate multilayer film by the clear contrast difference: dark Co-POM layers with heavy elements like W and Co along with bright GO layers with light elements like C and O (Figure 13c). The corresponding EELS analysis clearly distinguished the alternate GO and Co-POM layers within multilayer film owing to the high resolution of EELS at a subnanometer level (Figure 13d). Interestingly, the chemical contents also varied with respect to the position, highlighting a sequential layer-by-layer deposition of respective component. In specific,

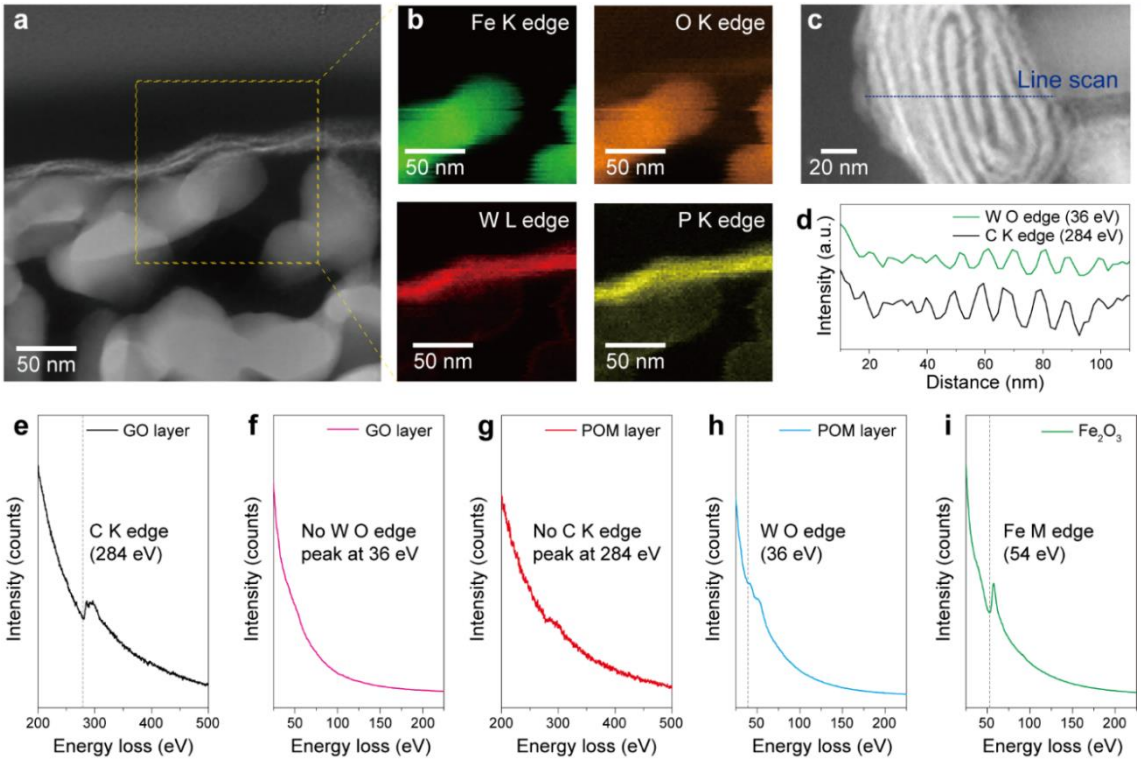

the peaks of the C K edge (284 eV) and the W O edge (36 eV) were alternately displayed with a clear contrast difference in a

Figure 13. STEM characterization of the $(GO/Co\text{-}POM)_9$ multilayer films. (a) Cross-sectional STEM image of the $(GO/Co\text{-}POM)_9$ multilayer films for EDS mapping (b) Elemental mapping of the $(GO/Co\text{-}POM)_9$ multilayer films, obtained from an EDS scan of the yellow box in panel (a). (c) High-magnification STEM image of the $(GO/Co\text{-}POM)_{10}$ multilayer films used for EELS analysis. (d) EELS line scan corresponding to the multilayer films. The blue and black lines correspond to the W and C, respectively, in GO and Co-POM layers extracted from the W O edge and C K edge peaks at 36 eV and 284 eV, respectively. (e-i) Extracted EELS data on different positions of multilayer: (e-f) C K edge and W O edge spectra on a GO layer, respectively; (g-h), C K edge and W O edge spectra on a Co-POM layer, respectively and (i) Fe M edge spectra on the hematite electrode.

distance span of approximately 4 nm (Figure 13 c, d). While only the peak at 284 eV determining the C K edge was clearly observed in the GO layer (Figure 13 g-h).Also, the peak at 54 eV corresponded to the unique Fe M edge in the hematite electrode (Figure 13i). Unlike the polymeric base layers which were difficult to identify due to the low contrast and the interpenetration of polymer chains, the $(GO/Co\text{-}POM)_9$ multilayer film clearly exhibited an artificial nacre-like structure with nanoscale alternate layers of organic and inorganic components, albeit with their large structural difference in the 2-dimensional GO and 0-dimensional Co-POM (hundreds of nm *vs*. 1-2 nm in diameter). The observed thickness difference between TEM and ellipsometry (about 4 *vs* 0.61 ± 0.05 nm per BL) could be originated from different surface roughness of the hematite electrode for STEM and the silicon wafer for ellipsometry.[34] It is previously reported that the deposition of nanoparticle-polyelectrolyte multilayer film can occur simultaneously *via* two different modes: (1) sequential deposition of dense monolayers and (2) formation of island layers followed by in-plane lateral deposition.[48] Based on the detailed STEM characterization, we verify that the alternate deposition of GO and Co-POM leads to the formation of artificial nacre-like hybrid film with nanoscale precision.

3-4. Photoelectrochemical Analysis of the Hematite Photoanode with the Catalytic Multilayers.

After confirming the successful growth of artificial nacre hybrid films of $(GO/Co\text{-}POM)_n$, they were subjected to the thermal reduction to engineer the performance of $(GO/Co\text{-}POM)_n$ multilayer films for water oxidation. It is well-known that thermal reduction of GO leads to an increase of its electrical conductivity, especially hole-transporting properties.[22,23] The 9 BL films were selected as a representative sample and reduced at three different temperatures of 100, 200, and 300 °C. The efficiency of the samples was evaluated by linear sweep voltammetry (LSV) with and without visible light illumination (Figure 14a). Even before the reduction, the hematite photoanode with the artificial nacre hybrid film exhibited a significantly improved performance in terms of both onset potential for water oxidation and photocurrent density, implying the catalytic

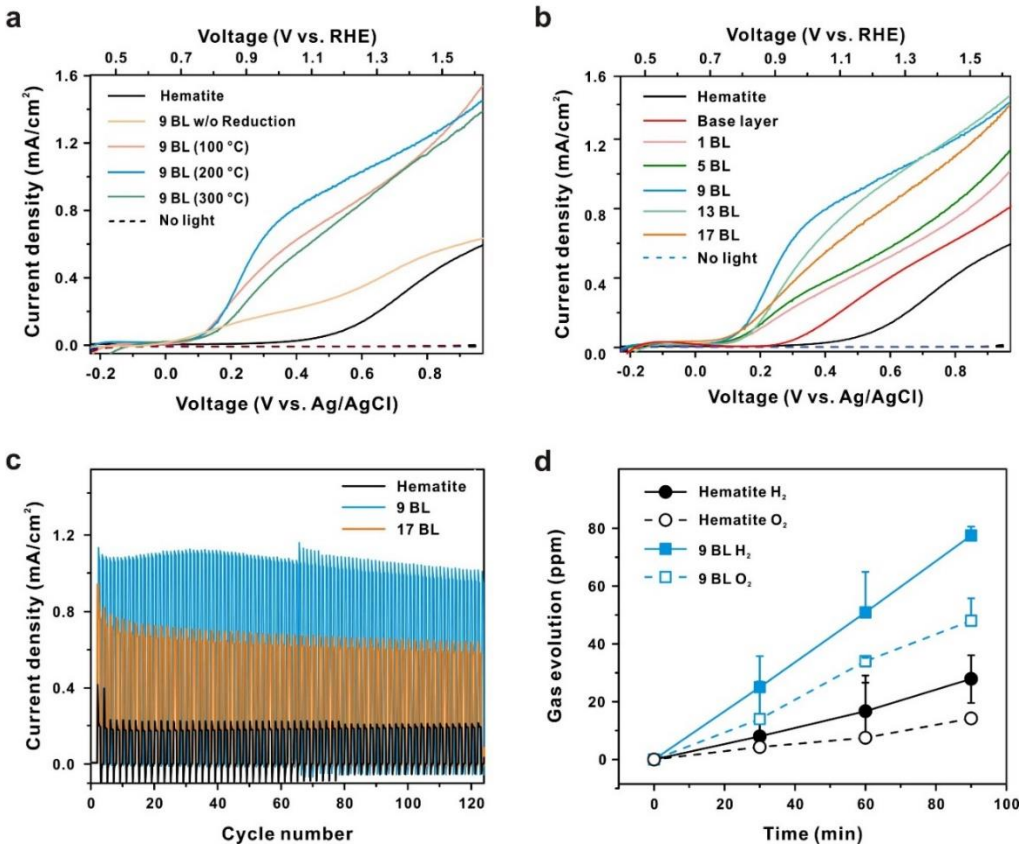

Figure 14. Photoelectrochemical performance of the hematite photoanode with the catalytic multilayers investigated by (a, b) LSV, (c) photocurrent measurement, and (d) gas chromatography. (a) Effect of the thermal reduction of GO on the performance of the hematite photoanode in the presence of the polymeric base layer $(PEI/PAA)_3$ and catalytic $(GO/Co\text{-}POM)_9$ multilayers as a representative film. (b) Influence of the number of the catalytic layers (BL, *n*). LSV curves were measured in a phosphate buffer solution (pH 8, 80 mM) in the presence (solid line) and absence (dashed line) of visible light irradiation. (c) Cycling test showing the long-term stability of the catalytic multilayer films of 9- and 17 BL under the applied bias of 1.23 V *vs.* RHE. (d) Time course of H_2 and O_2 gas evolution by the hematite photoanode with $(PEI/PAA)_3/(GO/Co\text{-}POM)_9$ film under visible light irradiation.

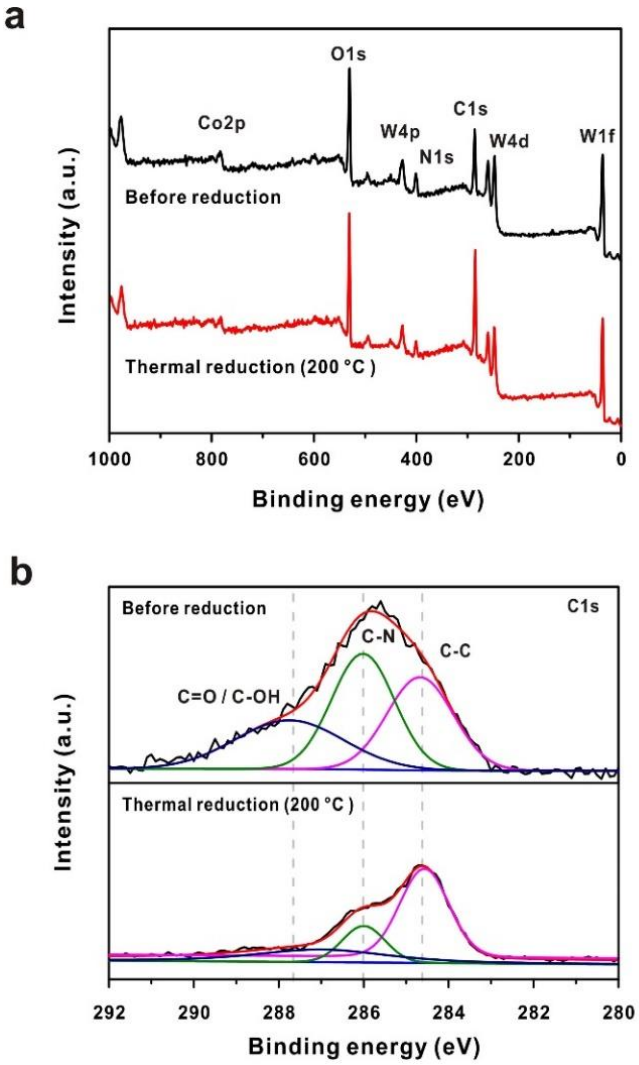

Figure 15. XPS analysis graph of (a, b) $(GO/Co\text{-}POM)_{17}$ on hematite electrode before and after thermal reduction at 200 °C. According to XPS analysis, the ratios of C/N and C/O were increased from 4.10 and 1.57 to 8.59 and 2.47, respectively, after the reduction. The deconvoluted high-resolution XPS spectra of carbon showed the decreased fraction of the C-N (286.0 eV), C=O and C-OH (287.7 eV), while that of the C-C (284.6 eV) maintained.

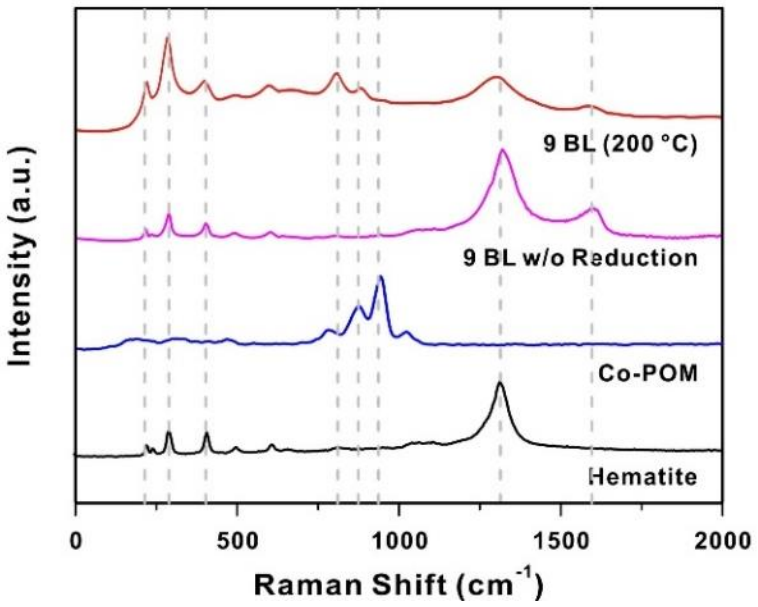

Figure 16. Raman spectrum of hematite, Co-POM and before and after reduction of $(GO/Co\text{-}POM)_9$ multilayer. This graph shows that the characterization peak of hematite (223, 291, 412, and 1318 cm^{-1}) and Co-POM (810, 900, and 968 cm^{-1}) is stably included after reduction. In addition, the reduction of GO is indicated by significantly decreased ratio D (1307.5 cm^{-1}) and G (1597.8 cm^{-1}) peak from 2.38 to 1.75.

effect of the hybrid film. X-ray photoelectron spectroscopy (XPS) and Raman spectroscopy both confirmed the successful reduction of GO and preservation of elemental distribution after the heat treatment (Figure 15 and Figure 16). It is found that the thermal reduction of GO has a negligible effect on the onset potential for water oxidation but has a significant effect on the increase of the photocurrent density of the hematite electrode, attributing to the improved electrical properties of GO upon reduction. The efficiency increased for samples treated at from 100 to 200 °C and then decreased at 300 °C. For example, the photocurrent densities of hematite electrodes assembled with $(GO/Co\text{-}POM)_9$ were found to be 0.49 (no treatment), 0.83 (100 °C), 1.03 (200 °C), and 0.78 mA cm^{-2} (300 °C), respectively, at an applied bias of 1.23 V *vs*. RHE electrode. It is believed that the dependence of the performance of the hematite photoanode on reduction temperatures is resulted from the compromise between the increased conductivity of the multilayer films and the thermal degradation of the polymeric base layers upon thermal reduction.

Based on these results, it was attempted to optimize the conditions for the catalytic multilayer assembly, enabling efficient and stable solar water oxidation by the hematite photoanode. When we investigated the effect of the number (n) of the catalytic $(GO/Co\text{-}POM)_n$, we found that 9 BL exhibited the best performance in terms of photocurrent density (Figure 17 and Figure 18). Although there was a negligible difference in the onset potential values between the samples with a different number of the catalytic multilayers (n ranges from 1 to 17 BL), there was a huge cathodic shift of the onset potential about 380 mV compared to the bare hematite. To the best of our knowledge, it is one of the largest cathodic shift of onset potential for the hematite photoanode, irrespective of measurement conditions such as pH, electrolyte concentration, and light intensity.[49]

Stability is another important issue in the photoelectrochemical cells. Thus, we performed the chronoamperometric cycling test to evaluate the stability of our catalytic multilayer films on the hematite electrode upon photoelectrochemical water oxidation. As shown in Figure 14c, the hematite electrode with our catalytic multilayer films exhibited a much higher photocurrent density compared to bare counterpart. It is noteworthy here that the $(GO/Co\text{-}POM)_9$ sample occasionally leads to gradual and abrupt increase of photocurrent density during the measurement unlike other samples. Considering that such phenomenon is frequently observed due to the formation and

detachment of gas bubbles in the active electrode,[50] we attribute it to a higher catalytic efficiency of the $(GO/Co\text{-}POM)_9$ sample. To further verify that the $(GO/Co\text{-}POM)_n$ multilayer films is indeed generating the oxygen and hydrogen gases from the hematite photoanode during the solar water oxidation, gas chromatography (GC) was used to measure the amount of the evolved gases under continuous visible light illumination (Figure 14d). The ratio of evolved hydrogen to oxygen was approximately 2.02 (± 0.19), and relative amount of evolved gases from the $(GO/Co\text{-}POM)_9$ sample was four times higher than the bare hematite electrode, confirming a higher efficiency and stability of the catalytic multilayers. Taken together the results from QCM, photocurrent, and GC analyses, the Faradaic efficiency and the turnover frequency of Co-POM were determined to be 68% and 6.93×10^2 h^{-1}, respectively, for the hematite electrode assembled with $(PEI/PAA)_3/(GO/Co\text{-}POM)_9$ catalytic layers.[49]

During the optimization, an unexpected role of the polymeric base layer was unveiled and found to contribute to the performance improvement of the hematite photoanode. Initially, the base layer was introduced prior to the assembly of the artificial nacre films of $(GO/Co\text{-}POM)_n$ to improve their adhesion to the hematite photoanode. Interestingly, the deposition of the base layer alone resulted in the increase of the photocurrent density and a slight cathodic shift of onset potential (Figure 14b). Encouraged by these findings, we systematically investigated the relationship between the number of polymeric base layer, the number of the catalytic multilayers, and the performance of the hematite photoanode in terms of photocurrent density. The pre-deposition of the base layer significantly improved the performance for photoelectrochemical water oxidation (Figure 17a and Figure 18). For example, the hematite photoanodes exhibited the best performance when both 3 BL of the base layer and 9 BL of the catalytic multilayer are deposited together. For the hematite with 9 BL of the catalytic multilayers, the current densities were found to be 1.03 and 0.51 mA/cm^2 at 1.23 V *vs.* RHE in the presence and absence of 3 BL of the base layer, respectively. To elucidate the underlying mechanism for the improvement, electrochemical impedance spectra (EIS) were evaluated (Figure 19b). EIS of the hematite electrode deposited with the base layer $(PEI/PAA)_3$ alone exhibited a smaller resistance for both charge transport in the hematite electrode (R_1) and electrocatalytic charge transfer (R_2) compared to the bare counterpart (Table 1).

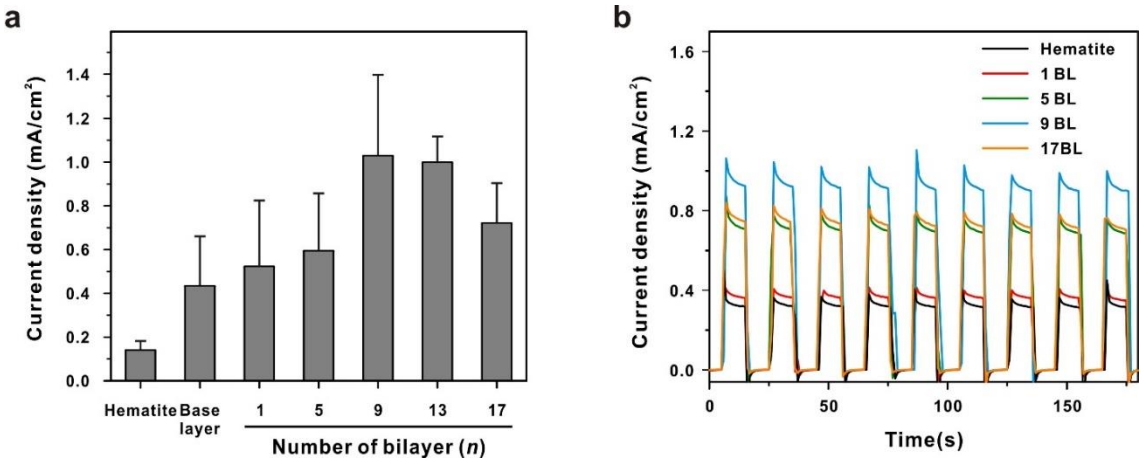

Figure 17. Photoelectrochemical performance graph. (a) Current density at hematite, base layer, $(GO/Co\text{-}POM)_n$ electrode at 0.56V and (b) chronoamperogram measured at short time intervals.

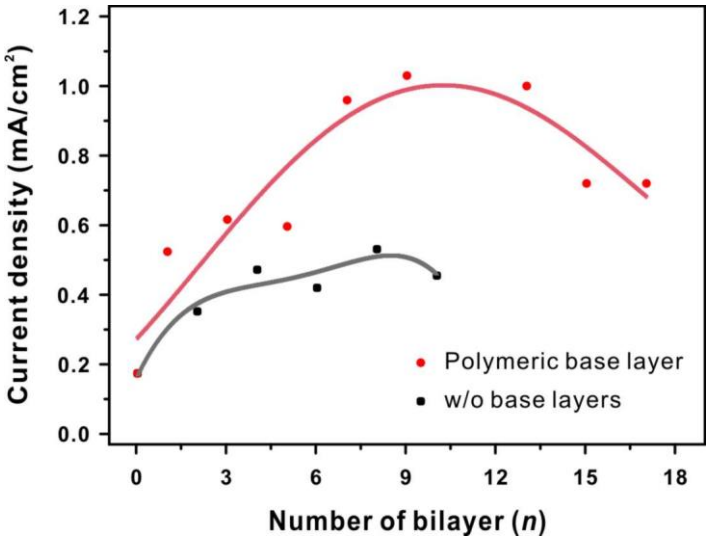

Figure 18. Graph representing the effect of polymeric base layer on density. The red line shows the difference in current density with number of catalytic multilayer when the polymeric base layer is deposited to 3 BL. On the other hand, the block line shows when there is no polymeric base layer.

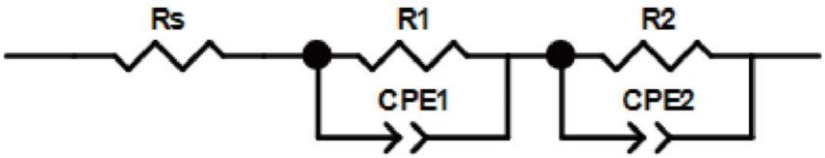

	Rs	R_1	R_2
		CPE1	CPE2
Hematite	34.93	609	21312
		4.36 E-6	1.53 E-4
Base layer	31.27	278	9729
		4.40 E-6	1.55 E-4
$(GO/Co\text{-}POM)_9$	3.40	26	895
		1.97 E-5	6.89 E-4
$(GO/Co\text{-}POM)_{17}$	40.77	305	10666
		4.90 E-6	1.70 E-4

Table 1. Equivalent circuit model used to fit the impedance data. R_1 and R_2 represents the charge transport in the hematite electrode and electrocatalytic charge transfer.

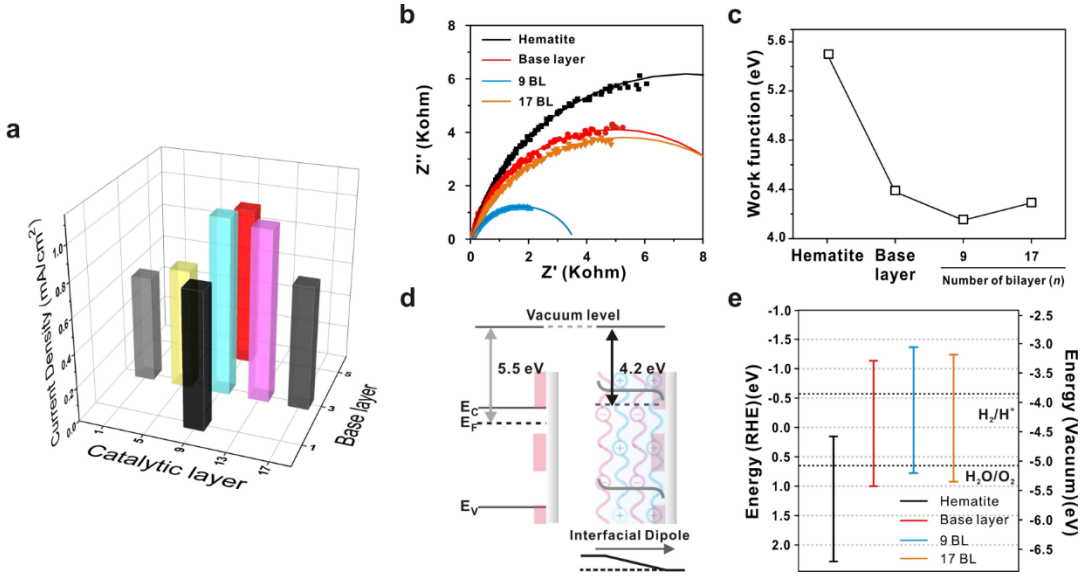

Figure 19. Energy level analysis of the hematite photoanode with the catalytic multilayers. (a) 3D-plot summarizing the tendency of current density to be controlled by number of catalytic bilayers and polymeric base layers. (b) Nyquist plots of impedance for hematite electrode assembled with catalytic multilayers, (c) The changes in work functions measured by UPS spectroscopy, (d) Scheme for reduced work function due to the dipole moment induced by polymeric base layers. (e) Energy diagram of all electrodes in this study. Band-bending is omitted for simplicity.

Further deposition of the catalytic multilayers led to even more significant decrease of them, demonstrating the respective role of GO and Co-POM as an efficient charge transporting material and an effective water oxidation catalyst. We hypothesize that the base layers contribute to the improvement by inducing band bending of hematite surface by its dipole moment and tuning the band-edge position more favorable for water oxidation (Figure 19d).

3-5 Energy level analysis of the hematite photoanode with the catalytic multilayers.

To support our hypothesis on the interfacial dipole effect of the polymeric base layers, we determined the work function of the hematite photoanode with and without the base layers and the catalytic multilayers by ultraviolet photoelectron spectroscopy (UPS) (Figure 19c-e and Figure 20). Deposition of polymeric base layers resulted in a significant decrease of work function from 5.5 to 4.4 eV (Figure 19c), indicating the presence of local dipole moment originating from the alternate layer of cationic and anionic materials. Our finding is consistent with recent reports[44–46] about the fabrication of low work-function electrode by the deposition of polyelectrolytes. Further deposition of 9 and 17 BL of the catalytic multilayers led to a more decrease of work function and thus more negative (i.e., upward) shift of the band-edge position (Figure 19d). Interestingly, the performance of the hematite photoanode was found to be inversely proportional to its work function, implying that the upward shift (or bending) of the band-edge potion is beneficial for water oxidation (Figure 19e). This observation is in consistent with the recent report on the relationship between the band-edge position and performance of photoanode.[51] This study is noteworthy in that GO, Co-POM and polymeric base layers are rationally assembled on hematite considering the energy level of each material and the effective charge transfer. GO as a hole transporting material offers conductive basement and Co-POM act as a water oxidation catalyst. In addition, the polymeric base layer effectively tuned the work function for enhanced catalytic dipole development. Finally, this process is also valuable in terms of that all experiments are fully-solution-processable and universally applicable.

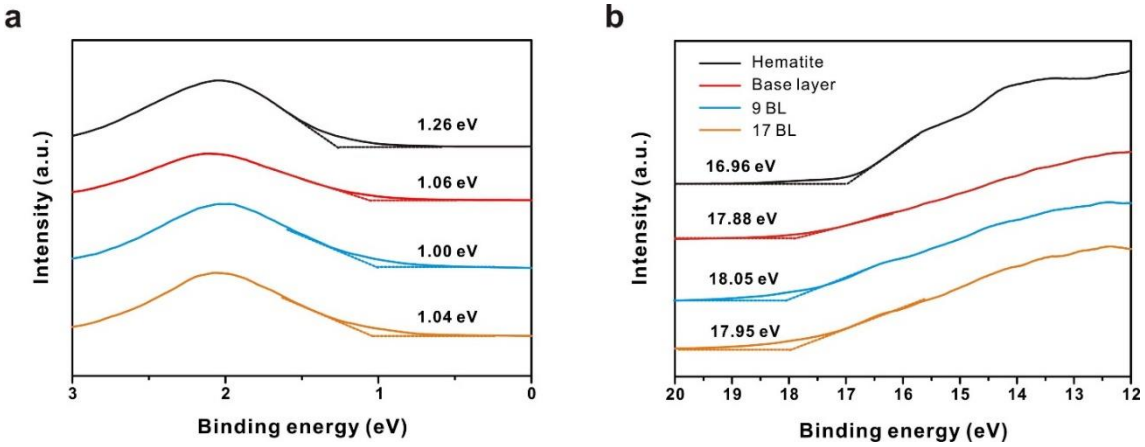

Figure 20. Ultraviolet photoelectron spectroscopy (UPS) spectra of hematite, base layer, $(GO/Co\text{-}POM)_9$ and $(GO/Co\text{-}POM)_{17}$ electrodes. (a) Fermi level and (b) cut-off level analysis of electrodes.

IV. Conclusion

In summary, we developed a novel nacre-like catalytic multilayers that integrate GO and Co-POM by layer-by-layer assembly for improvement on artificial photosynthetic efficiency of hematite electrode. This catalytic multilayer was precisely optimized by the amount of catalysts through adjusting the number of catalytic multilayers as well as additional heat treatment condition for high photocatalytic efficiency. The hematite electrode assembled with catalytic multilayers showed superior photocatalytic activity compared with a bare hematite electrode, indicating that the catalytic multilayers plays an important role in the effective hole transfer to the water. Moreover, the polymeric base layer which was introduced to artificial photosynthetic system for the first time affected crucial influence in photocatalytic performance through the surface dipole, band banding effect and work function tuning. We anticipate that this study will provide a platform to design for developing a high-performance artificial photosynthetic photoanode.

V. References

(1) Pérez-Lombard, L.; Ortiz, J.; Pout, C. *Energy Build.* **2008**, *40*, 394–398.

(2) Yan, L.; Chang, Y. N.; Yin, W.; Tian, G.; Zhou, L.; Hu, Z.; Xing, G.; Gu, Z.; Zhao, Y. *Adv. Eng. Mater.* **2015**, *17*, 523–531.

(3) McEvoy, J. P.; Brudvig, G. W. *Chem. Rev.* **2006**, *106*, 4455–4483.

(4) Renger, G.; Renger, T. *Photosynth. Res.* **2008**, *98* (1–3), 53–80.

(5) Lubitz, W.; Reijerse, E. J.; Messinger, J. *Energy Environ. Sci.* **2008**, *1*, 15.

(6) Kärkäs, M. D.; Verho, O.; Johnston, E. V.; Åkermark, B. *Chem. Rev.* **2014**, *114*, 11863–12001.

(7) Meng, F.; Li, J.; Cushing, S. K.; Bright, J.; Zhi, M.; Rowley, J. D.; Hong, Z.; Manivannan, A.; Bristow, A. D.; Wu, N. *ACS Catal.* **2013**, *3*, 746–751.

(8) Ryu, J.; Lee, S. H.; Nam, D. H.; Park, C. B. *Adv. Mater.* **2011**, *23*, 1883–1888.

(9) Lee, H. Y.; Ryu, J.; Kim, J. H.; Lee, S. H.; Park, C. B. *ChemSusChem* **2012**, *5*, 2129–2132.

(10) Jang, J.-W.; Du, C.; Ye, Y.; Lin, Y.; Yao, X.; Thorne, J.; Liu, E.; McMahon, G.; Zhu, J.; Javey, A.; Guo, J.; Wang, D. *Nat. Commun.* **2015**, *6*, 7447.

(11) Kim, J. Y.; Jang, J. W.; Youn, D. H.; Magesh, G.; Lee, J. S. *Adv. Energy Mater.* **2014**, *4*, 1–7.

(12) Jang, J.-W.; Du, C.; Ye, Y.; Lin, Y.; Yao, X.; Thorne, J.; Liu, E.; McMahon, G.; Zhu, J.; Javey, A.; Guo, J.; Wang, D. *Nat. Commun.* **2015**, *6*, 7447.

(13) Barthelat, F. *Bioinspir. Biomim.* **2010**, *5*, 35001.

(14) Yeom, B.; Sain, T.; Lacevic, N.; Bukharina, D.; Cha, S.-H.; Waas, A. M.; Arruda, E. M.; Kotov, N. A. *Nature* **2017**, *543*, 95–98.

(15) Wan, S.; Peng, J.; Li, Y.; Hu, H.; Jiang, L.; Cheng, Q. *ACS Nano* **2015**, *9*, 9830–9836.

(16) Yao, H. Bin; Tan, Z. H.; Fang, H. Y.; Yu, S. H. *Angew. Chem. Int. Ed.* **2010**, *49*,

10127–10131.

(17) Finnemore, A.; Cunha, P.; Shean, T.; Vignolini, S.; Guldin, S.; Oyen, M.; Steiner, U. *Nat. Commun.* **2012**, *3*, 966.

(18) Wei, H.; Ma, N.; Shi, F.; Wang, Z.; Zhang, X. *Chem. Mater.* **2007**, *19*, 1974–1978.

(19) Tamirat, A. G.; Rick, J.; Dubale, A. A.; Su, W.-N.; Hwang, B.-J. *Nanoscale Horiz.* **2016**, *1*, 243–267.

(20) Hisatomi, T.; Dotan, H.; Stefik, M.; Sivula, K.; Rothschild, A.; Grätzel, M.; Mathews, N. *Adv. Mater.* **2012**, *24*, 2699–2702.

(21) Formal, F. Le; Grätzel, M.; Sivula, K. *Adv. Funct. Mater.* **2010**, *20*, 1099–1107.

(22) Jung, I.; Dikin, D. A.; Piner, R. D.; Ruoff, R. S. *Nano Lett.* **2008**, *8*, 4283–4287.

(23) Lee, D. W.; Hong, T.-K.; Kang, D.; Lee, J.; Heo, M.; Kim, J. Y.; Kim, B.-S.; Shin, H. S. *J. Mater. Chem.* **2011**, *21*, 3438–3442.

(24) Yin, Q.; Tan, J. M.; Besson, C.; Geletii, Y. V; Musaev, D. G.; Kuznetsov, A. E.; Luo, Z.; Hardcastle, K. I.; Hill, C. L. *Science* **2010**, *328*, 342–345.

(25) Ismail, A. A.; Bahnemann, D. W. *Sol. Energy Mater. Sol. Cells* **2014**, *128*, 85–101.

(26) FUJISHIMA, A.; HONDA, K. *Nature* **1972**, *238*, 37–38.

(27) Chen, J.-J.; Wu, J. C. S.; Wu, P. C.; Tsai, D. P. *J. Phys. Chem. C* **2011**, *115*, 210–216.

(28) Liu, J.; Liu, Y.; Liu, N.; Han, Y.; Zhang, X.; Huang, H.; Lifshitz, Y.; Lee, S.-T.; Zhong, J.; Kang, Z. *Science* **2015**, *347*, 970–974.

(29) Xie, G.; Zhang, K.; Guo, B.; Liu, Q.; Fang, L.; Gong, J. R. *Adv. Mater.* **2013**, *25*, 3820–3839.

(30) Brillet, J.; Grätzel, M.; Sivula, K. *Nano Lett.* **2010**, *10*, 4155–4160.

(31) Ng, Y. H.; Iwase, A.; Kudo, A.; Amal, R. *J. Phys. Chem. Lett.* **2010**, *1*, 2607–

2612.

(32) Cao, L.; Sahu, S.; Anilkumar, P.; Bunker, C. E.; Xu, J.; Fernando, K. A. S.; Wang, P.; Guliants, E. A.; Tackett, K. N.; Sun, Y. P. *J. Am. Chem. Soc.* **2011**, *133*, 4754–4757.

(33) Ahn, E.; Lee, T.; Gu, M.; Park, M.; Min, S. H.; Kim, B. S. *Chem. Mater.* **2017**, *29*, 69–79.

(34) Ahn, E.; Kim, B.-S. *ACS Appl. Mater. Interfaces* **2017**, *9*, 8688–8695.

(35) Guo, H.; Guo, Q.; Chu, T.; Zhang, X.; Wu, Z.; Yu, D. *J. Mater. Sci. Mater. Med.* **2014**, *25*, 121–129.

(36) Park, M.; Lee, T.; Kim, B.-S. *Nanoscale* **2013**, *5*, 12255–12260.

(37) Park, M.; Song, K.; Lee, T.; Cha, J.; Lyo, I.; Kim, B. S. *ACS Appl. Mater. Interfaces* **2016**, *8*, 21595–21602.

(38) Gu, M.; Kim, B. S. *Nano Energy* **2016**, *30*, 658–666.

(39) Joo, P.; Jo, K.; Ahn, G.; Voiry, D.; Jeong, H. Y.; Ryu, S.; Chhowalla, M.; Kim, B. S. *Nano Lett.* **2014**, *14*, 6456–6462.

(40) Bao, H.; Pan, Y.; Ping, Y.; Sahoo, N. G.; Wu, T.; Li, L.; Li, J.; Gan, L. H. *Small* **2011**, *7*, 1569–1578.

(41) Wang, S. S.; Yang, G. Y. *Chem. Rev.* **2015**, *115*, 4893–4962.

(42) Toma, F. M.; Sartorel, A.; Iurlo, M.; Carraro, M.; Parisse, P.; Maccato, C.; Rapino, S.; Gonzalez, B. R.; Amenitsch, H.; Da Ros, T.; Casalis, L.; Goldoni, A.; '*Nat. Chem.* **2010**, *2*, 826–831.

(43) Xu, S.; Wang, Y.; Zhao, Y.; Chen, W.; Wang, J.; He, L.; Su, Z.; Wang, E.; Kang, Z. *J. Mater. Chem. A* **2016**, *4*, 14025–14032.

(44) Zhou, Y.; Fuentes-hernandez, C.; Shim, J.; Meyer, J.; Giordano, A. J.; Li, H.; Winget, P.; Papadopoulos, T.; Cheun, H.; Kim, J.; Fenoll, M.; Dindar, A.; Haske, W.; Najafabadi, E.; Khan, T. M.; Sojoudi, H.; Barlow, S.; Graham, S.; Brédas, J.; Marder, S. R.; Kahn, A.; Kippelen, B. **2012**, *873*, 327–332.

(45) Lee, B. R.; Lee, S.; Park, J. H.; Jung, E. D.; Yu, J. C.; Nam, Y. S.; Heo, J.; Kim, J. Y.; Kim, B. S.; Song, M. H. *Adv. Mater.* **2015**, *27*, 3553–3559.

(46) Torasso, N.; Armaleo, J. M.; Tagliazucchi, M.; Williams, F. J. *Langmuir* **2017**, *33*, 2169–2176.

(47) Hwang, H.; Joo, P.; Kang, M. S.; Ahn, G.; Han, J. T.; Kim, B. S.; Cho, J. H. *ACS Nano* **2012**, *6*, 2432–2440.

(48) Ostrander, J. W.; Mamedov, A. A.; Kotov, N. A. *J. Am. Chem. Soc.* **2001**, *123*, 1101–1110.

(49) Li, H.; Liu, R.; Kong, W.; Liu, J.; Liu, Y.; Zhou, L.; Zhang, X.; Lee, S.-T.; Kang, Z. *Nanoscale* **2014**, *6*, 867–873.

(50) Clément, N.; Nishiguchi, K.; Dufreche, J. F.; Guerin, D.; Fujiwara, A.; Vuillaume, D. *Nano Lett.* **2013**, *13*, 3903–3908.

(51) Wu, H.; Ren, F.; Xing, Z.; Zheng, X.; Wu, L.; Jiang, C. *J. Appl. Phys.* **2017**, *121*.

Acknowledgements

아직 배울 것이 많이 남은 것 같은데 벌써 2 년이란 시간이 흘러 졸업을 앞두게 되었습니다. 짧다면 짧고 길다면 긴 석사과정 동안 연구실에서 좋은 사람들과 재미있는 연구를 진행할 수 있어서 힘들었지만, 또한 즐거웠습니다. 학위 과정 동안 제게 많은 도움을 주신 분들과 저를 응원해 주신 분들께 학위논문 한쪽에 감사의 마음을 담아 글을 적습니다.

먼저 부족했던 저를 받아주시고 연구의 길로 이끌어주신 지도교수님이신 김병수 교수님께 진심으로 감사드립니다. 항상 열정적이시고 따뜻하신 교수님과 함께였기에 무사히 학위과정을 마칠 수 있었습니다. 다시 한번 고개 숙여 감사드립니다. 그리고 고민 많던 학부 과정 때부터 다사다난하였던 석사과정까지 많은 인생의 조언을 하여 주신 권태혁 교수님과 부족한 저를 이끌고 함께 연구하여 주신 류정기 교수님께도 진심으로 감사드립니다.

KBS 연구실 식구들에게도 감사드립니다. 지금은 연구교수님이 되신 저의 영원한 사수 유리 누나, 졸업 준비로 바쁘신 와중에도 많은 것들을 가르쳐 주신 태민이 형, Cryo TEM 을 배울 기회를 주신 은용이 형, 항상 친형처럼 큰일 작은일 하나하나 챙겨주었던 응진이 형, LG 화학에서 다시 만나고 싶은 준희 형, 연구로 어려워하던 시절에 손 내밀어 준 민수형, 후배들에게 따뜻하게 대해 준 밥 대장 이슬 누나, 처음에 존댓말로 시작했지만 이제는 친구가 된 민주, 학위과정 동안 깊은 얘기 많이 나눈 균혁이, 회사에서 원하는 인재인 싹싹한 송아, 졸업이 다가오며 점점 밝아지는 재은이, 어딜 가도 잘 할거 같은 해리, 함께 연구실 생활을 시작한 민성이, 연구실 짬으로는 박사과정인 태형이, 꼼꼼하고 착실한 윤경이, 롤 대장 은별이, 새로 연구실에 들어올 동석, 영주, 함께해서 즐거웠던 재원이, 금석이. 저는 졸업을 하여 연구실을 떠나지만 앞으로도 좋은 인연 계속 이어나갔으면 좋겠습니다.

그리고 울산으로 떠난 친구를 멀리서 응원해 준 중학교 동창 원혁, 정욱, 주남, 한규, 성국 그리고 고등학교 친구인 민제, 수호, 상봉, 인경, 호준, 진민, 성찬, 희현, 정우, 세연, 지헌이, 힘들 때 술 한잔 같이 해 준 대학 친구 종석이, 진영이, 09 학번 룸메 태희형, 용진이형, 명준이형, 민이형, 진수형, 성현이형, 진솔이형, 이름이형, 타지에서 서로 의지하며 함께 대학 생활을 보낸 현지 모두 고맙습니다. 끝으로 저를 항상 믿어주고 힘들 때 버팀목이 되어주는 사랑하는 가족 아버지와 어머니, 누나, 매형, 조카 이현이에게 감사의 말을 전합니다.